

Article

NIR-MID Reflectance and Emissivity Study at Different Temperatures of Sodium Carbonate Minerals: Spectra Characterization and Implication for Remote Sensing Identification

Maximiliano Fastelli ^{1,*}, Azzurra Zucchini ¹ , Paola Comodi ¹, Alessandro Maturilli ² , Giulia Alemanno ², Ernesto Palomba ³ and Riccardo Piergallini ⁴

¹ Dipartimento di Fisica e Geologia, Università degli Studi di Perugia, 06123 Perugia, Italy; azzurra.zucchini@unipg.it (A.Z.); paola.comodi@unipg.it (P.C.)

² Institute of Planetary Research, DLR, German Aerospace Centre, D-12489 Berlin, Germany; alessandro.maturilli@dlr.de (A.M.); giulia.alemanno@dlr.de (G.A.)

³ Istituto di Astrofisica e Planetologia Spaziali, Istituto Nazionale di Astrofisica (INAF), 00136 Rome, Italy; ernesto.palomba@inaf.it

⁴ School of Science and Technology, University of Camerino, 62032 Camerino, Italy; riccardo.piergallini@unicam.it

* Correspondence: maximiliano.fastelli@studenti.unipg.it



check for updates

Citation: Fastelli, M.; Zucchini, A.; Comodi, P.; Maturilli, A.; Alemanno, G.; Palomba, E.; Piergallini, R. NIR-MID Reflectance and Emissivity Study at Different Temperatures of Sodium Carbonate Minerals: Spectra Characterization and Implication for Remote Sensing Identification. *Minerals* **2021**, *11*, 845. <https://doi.org/10.3390/min11080845>

Academic Editors: Yasuhiro Sekine and Jesus Martinez-Frias

Received: 26 May 2021

Accepted: 31 July 2021

Published: 5 August 2021

Publisher's Note: MDPI stays neutral with regard to jurisdictional claims in published maps and institutional affiliations.



Copyright: © 2021 by the authors. Licensee MDPI, Basel, Switzerland. This article is an open access article distributed under the terms and conditions of the Creative Commons Attribution (CC BY) license (<https://creativecommons.org/licenses/by/4.0/>).

Abstract: Recent satellite observations and the deconvolution of remote sensing data have shown the existence of various carbonate minerals in different solar system bodies. Emissivity, from 403 to 803 K, and reflectance spectra at 300 and 193 K of selected carbonates minerals with different ratios of Na:Ca and water amounts were respectively collected at 3–20 μm and at 1–16 μm . All reflectance spectra show absorption features in the 1.9–2.5 and 3.4–4.0 μm areas due to overtone and a combination of CO_3^{2-} and fundamental vibrational models at ≈ 9.09 , 11.35, 7.06, and 14.7 μm . The increase of the Na:Ca ratio in anhydrous samples produces a shift of the absorption features in the 3.4–4.0 μm area toward shorter wavelengths, and the peak at 3.9 μm doubles in the presence of a CO_3^{2-} oxygen group shared with two cations in minerals having more complex structures. The comparison of the bands at ≈ 669 and ≈ 794 cm^{-1} in the emissivity spectra collected at high temperatures indicates that around 600 K, phase transitions occurred in natrite and thermonatrite. The reflectance spectra measured at 193 K reveal a fine structure compared to spectra collected at room temperature. The comparison of laboratory results with the spectrum of Ceres's brightest crater Occator from the Dawn mission, taken as a case study, showed how the anhydrous samples, shortite and nyerereite, studied in this work can also be hypothesized for Ceres's surface beyond that already suggested (trona, natrite, thermonatrite).

Keywords: emissivity; reflectance; carbonates; mineralogy; icy bodies

1. Introduction

Near-infrared spectroscopy (NIR) and mid-infrared spectroscopy (MID) permit the identification of minerals according to their compositional/structural properties. The assignment of experimental data to remote sensing observations of planetary body surfaces (e.g., [1–3]) is of paramount importance to detect the mineralogical composition of the surfaces of planetary bodies in the solar system.

Carbonates are relevant minerals to understand the surface composition of several planetary bodies and are crucial environmental markers. Some lines of evidence indicate that different types of carbonate minerals that occur on the surface of Mars, Ceres, Enceladus, and Europa [4–19].

Carbonates were detected on the Martian surface through remote sensing techniques and in situ observations by rovers [4,5]. The presence of carbonates on the surface

is attested by many spectral evidences; e.g., Compact Reconnaissance Imaging Spectrometer for Mars (CRISM) detected carbonates in Noachian terrains using near-infrared reflectance [5]. These minerals have been also discovered at the Phoenix and Gusev landing sites [6,7]. Carbonate is an expected weathering product of water and basalt in an atmosphere with CO₂ [20]. They are important records of fluid activity in the Martian surface and water–rock system interaction in relation to potentially living systems in the ancient past of Mars [21].

Ceres's spectrum shows a diagnostic carbonate signature in the area at 3.3–4 μm confirmed by the Dawn mission [8]. The average surface of Ceres is composed of phyllosilicate, ammonium-bearing minerals, Mg-Ca carbonates, water ice, and salts [10]. A large amount of Na-carbonate is present in the brightest area in Ceres's Occator crater [9]. The spectral fit of the Occator bright spot presents natrite (Na₂CO₃), mixed with other elements, as the best carbonate mineral candidate [9]. Carbonates was also found on Ahuna Mons [11] and on additional bright faculae distributed on Ceres's surface [8]. Carrozzo et al. [8] report the additional presence of hydrate forms of sodium carbonate such as thermonatrite (Na₂CO₃·H₂O) and trona [Na₃(CO₃)(HCO₃)·2(H₂O)]. The main hypothesis for the formation of bright spots is the minerals' genesis from the liquid brine reservoir, i.e., the material produced by impacts that induce heating of the surface brine [12]. By the above-mentioned results, Ceres's dwarf planet has been included in the category of celestial bodies with possible oceans underneath the crust (e.g., Europe, Ganymede, Callisto) [12,13].

The surface composition of Enceladus has some analogies with that of Ceres; in fact, plumes erupted by Enceladus are formed of ammonium-bearing minerals, water, and carbonate salts such as NaHCO₃ and NaCO₃ [14]. The genesis of these salts is attributed to the presence of oceans underneath the surface rich in Na elements [15].

Moreover, hydrated sulfate and carbonate minerals are the principal candidates for composing the wide non-icy part of the Europa surface, which is the second Galilean satellite outward from Jupiter [16,17]. Recently, De Angelis et al. [18] showed how the spectra of some hydrated Na-carbonate minerals strongly match with reflectance spectra remotely coming from Europa. Magnesium and sodium sulfates, sodium carbonate, and a mixture of these salts provided a good fit for the non-ice material [19]. Zolotov et al. [22] demonstrate how hydrated salts are thermodynamically stable in ice-bearing deposits on the surface of Europa.

The origin of the hydrated sulfates and sodium carbonate minerals on the surface of Jovian moons was attributed to the base of the density analogy between the bulk icy satellites and the CI carbonaceous chondrites [23–25]: the icy satellites were supposed to be accreted from CI chondrite during primordial stages of heating that caused the decomposition of carbonates (formed by oxidation of organics) and CO₂ degassing. The icy shell and possibly the ocean tend to trap the CO₂, which would be available to drive the formation of carbonates and bicarbonates [25].

On Earth, alkaline carbonate minerals are often attributed to a magmatic origin even if they were also found in carbonatite deposits as melt inclusions [26]. Na-Ca carbonates were discovered in natrocarbonatite magmas erupted by the Oldoinyo Lengai volcano (East African Rift System, northern Tanzania), which is the only active carbonatite volcano on Earth [27,28].

Nyerereite and shortite (attributed to the subsolidus breakdown of nyerereite) were identified in mantle-derived melt inclusions in kimberlites ([29–32] and references therein) as well as in minerals from multiphase solid inclusions in diamonds [33].

The occurrence of alkaline carbonates both in natrocarbonatite magmas and in deep-mantle derived products is of paramount importance as it offers unique insight into the interior of the Earth, i.e., the composition and origin of kimberlites and mantle-derived melts and deep Earth composition.

Recently, natrocarbonates have attracted the attention of the scientific community as they have been found to play a key role in carbon capture and storage acting as CO₂ trapping by mineral carbonation. [34].

An interesting topic is the chemical composition and structure of the icy planets in relation to the presence of oceans underneath the crust, as the strong interaction between oceanic crust and the surface is crucial for their habitability. The occurrence of the mineral phases listed above gives important indications about the internal dynamic of the icy planetary bodies [35], as their presence is closely related to variation in pressure (P) and temperature (T) during the evolution of these bodies. Indeed, fluid and volatile storage are functions of P/T conditions inside minerals' structure, according to the topological changes in crystalline structures [36]. Consequently, to elaborate hypotheses about the depth of one or more oceans, as well as the thickness of the ice crust, it is necessary to focus on the behavior of non-ice components and their evolution under the crust of an icy planet. Moreover, phase transitions occurring under different pressure and temperature conditions can drastically change the mineral density and can affect the buoyancy and internal dynamics of planetary bodies [37–39].

Several studies report carbonate measurements in the laboratory e.g., [40], using VIS-NIR reflectance spectroscopy, although there are very few investigated carbonates at non-ambient temperature. In some cases, researchers have also not collected data in the spectral range larger than 5 μm. Gaffey [41] reports reflectance spectra of anhydrous carbonate minerals in the 0.35–2.55 μm range. Some literature data e.g., [42] focused on the study of natrite (NaCO₃) reflectance spectra at various temperature and in the spectral range up to 25 μm, taking into account the phase transitions at high temperature of this phase [43]. Recently, De Angelis et al. [18] analyzed the reflectance spectra of Na-carbonates (1–4.8 μm) at cryogenic temperature (down to 90 K). Notwithstanding the abundant literature on natrocarbonates spectroscopic studies, the whole set of alkaline and earth-alkaline carbonate minerals reflectance spectra has not been covered. For nyerereite, only Raman spectra [44] is reported, even though this mineral is very important in the geological scenario, as previously documented, and likely having an important role also in the planetary context.

A set of hydrated and anhydrous Na-Ca carbonate minerals, which should be relevant to the planetological context, has been selected for this work. The aims of this project are as follows: (1) to improve the spectral libraries of carbonate minerals with reflectance and emissivity spectra at different temperatures and wide spectral range; (2) to understand how crystal–chemical changes affect the spectral features in each sample; (3) to evaluate temperature changes such as dehydration and/or phase transitions; (4) to compare new anhydrous carbonates (shortite and nyerereite) to Ceres's surface; and (5) to present a new algorithm to compare remote sensing data collected by spacecraft satellites with laboratory measured spectra of selected mineral mixtures.

X-ray diffraction analyses were performed on the selected samples before and after thermal treatments to study the evolution of their crystal structure. The spectral evolution was also studied in a wide temperature range, from 193 K to around 803 K, for all samples (except for nyerereite for which we only have reflectance data).

Once we analyzed the minerals spectra and their evolutions with *T*, we applied our data to a case study, the Ceres Cerealia bright spot taken from [45]. A quantitative fitting of the spectra coming from this area and collected from the Dawn mission was performed by using an algorithm, *mixture fit*, based on the Hapke model [46,47] and working by applying an areal (linear) mixing. The detailed procedure is reported in Appendix A.

Spectroscopy Properties of CO_3^{2-} and $\text{H}_2\text{O}/\text{OH}$ Groups

The free CO_3^{2-} ion (D_{3h} symmetry) has four fundamental IR-active vibrational modes: symmetric stretching (ν_1), out-of-plane bend (ν_2), degenerate antisymmetric stretch (ν_3), and degenerated bending mode (ν_4) [48]. Generally, strong IR modes appear near 1100 cm^{-1} due to the symmetric stretching vibration (ν_1) and at $7.14\text{ }\mu\text{m}$ (1400 cm^{-1}) generated to antisymmetric stretch (ν_3). Absorption bands near $12.5\text{ }\mu\text{m}$ (800 cm^{-1}) are due to out-of-plane bend (ν_2), while features around $14.28\text{ }\mu\text{m}$ (700 cm^{-1}) are due to in-plane bending modes (ν_4) [49]. Overtone and combinations of CO_3^{2-} are expected in the areas at $1.85\text{--}1.87\text{ }\mu\text{m}$ ($\nu_1 + 3\nu_3$), $1.97\text{--}2.00\text{ }\mu\text{m}$ ($2\nu_1 + 2\nu_3$), $2.12\text{--}2.16\text{ }\mu\text{m}$ ($3\nu_1 + 2\nu_4$), $2.30\text{--}2.35\text{ }\mu\text{m}$ ($3\nu_3$), and $2.50\text{--}2.55\text{ }\mu\text{m}$ ($\nu_1 + 2\nu_3$) [50]. Absorption features located in the range from 3.40 to $4.00\text{ }\mu\text{m}$ ($29412\text{--}500\text{ cm}^{-1}$) can be assigned to combination and vibrational modes due to $\nu_2 + \nu_4/2\nu_2 + \nu_4/\nu_3$ [51]. H_2O free molecule has three fundamental vibrational modes: at $2.73\text{ }\mu\text{m}$ (3657 cm^{-1}) (ν_1) symmetric stretching, $6.26\text{ }\mu\text{m}$ (1595 cm^{-1}) (ν_2) symmetric bending, and at $2.66\text{ }\mu\text{m}$ (3756 cm^{-1}) (ν_3) asymmetric stretching [52]. The free HCO_3^- ion has also four modes: ν_1 symmetric stretching at $9.04\text{ }\mu\text{m}$ (1063 cm^{-1}), ν_2 symmetric bending at $11.37\text{ }\mu\text{m}$ (879 cm^{-1}), ν_3 asymmetric stretching at $7.06\text{ }\mu\text{m}$ (1415 cm^{-1}), and ν_4 asymmetric bending at $14.7\text{ }\mu\text{m}$ (680 cm^{-1}). The H_2O free molecule presents a symmetric H-O-H stretch at $2.73\text{ }\mu\text{m}$ (3663 cm^{-1}), an asymmetric H-O-H stretch at $2.66\text{ }\mu\text{m}$ (3759 cm^{-1}), H-O-H bending at $6.27\text{ }\mu\text{m}$ (1594 cm^{-1}) [53], and a rotational fundamental band at $20\text{ }\mu\text{m}$ (500 cm^{-1}) [54]. OH has a single stretching vibration, near $2.8\text{ }\mu\text{m}$ (3571 cm^{-1}). The overtones of these vibrational modes are expected near $1.4\text{ }\mu\text{m}$ and $0.45\text{ }\mu\text{m}$ (7142 and $22,222\text{ cm}^{-1}$) [55]. OH also has rotational vibration bands in the $9.2\text{--}5\text{ }\mu\text{m}$ ($1086\text{--}400\text{ cm}^{-1}$) range and translational vibration bands in the $1.5\text{--}3.3\text{ }\mu\text{m}$ ($666\text{--}303\text{ cm}^{-1}$) range [56]. Peaks located around $1.9\text{ }\mu\text{m}$ (5263 cm^{-1}) are defined as water combination bands, whereas the strongest OH overtones are in the region $1.38\text{--}1.41\text{ }\mu\text{m}$ ($7246\text{--}7092\text{ cm}^{-1}$) [57]. The $3\text{ }\mu\text{m}$ (3333 cm^{-1}) region of all the spectra shows well-defined H_2O stretching fundamental bands. The minerals examined in this manuscript have H_2O in structurally different sites, as explained carefully below, and they are involved in hydrogen bonds (mention as H_2O^+), which may have different lengths and resistances sensitive to both temperature and crystalline structure.

2. Materials and Methods

2.1. Samples

We analyzed the samples reported in Table 1.

Table 1. Chemical formula, minerals name, and source for selected samples used in this work.

Minerals	Chemical Formula	Source
Natrite	Na_2CO_3	Koashva, Kola, Russia
Nyerereite	$\text{Na}_2\text{Ca}(\text{CO}_3)_2$	Synthetic
Shortite	$\text{Na}_2\text{Ca}_2(\text{CO}_3)_3$	Green River, Wyoming, USA
Thermonatrite	$\text{Na}_2\text{CO}_3 \cdot \text{H}_2\text{O}$	MT. Koashva, Kola, Russia
Trona	$\text{Na}_2(\text{CO}_3)(\text{HCO}_3) \cdot 2(\text{H}_2\text{O})$	Wadi El-Natron, Western Desert, Egypt

Reflectance and emissivity measurements on the proposed samples were performed at the PSL (Planetary Spectroscopy Laboratory, DLR, Berlin, Germany).

2.2. Emissivity and Reflectance Measurements

At PSL, two identical Bruker Vertex 80 V FTIR spectrometers are equipped, each with an external emissivity chamber. The chamber used for medium-low temperature (from 303 to 343 K) emissivity measurements is continuously purged with dry air (atmospheric water and CO_2 removed) at room pressure. A second emissivity chamber, which can be evacuated at 0.7 mbar s, to obtain measurements free of atmospheric spectral feature [58], and is directly attached to the second spectrometer, allows measuring the emissivity

of samples under vacuum at high temperature, up to approximately 803 K. Under this vacuum emissivity setup, the entire stainless-steel cup is heated up using an induction system, allowing heating the samples from below as well as from the side of the cup. The temperature was measured by a thermocouple in contact with the emitting source. The emissivity spectra were scaled by a comparison with the blackbody emission spectrum measured at the same temperature and under the same setup configuration. Details on the emissivity measurements can be found in [38].

Details on the reflectance collection process and PSL build-up are described in [38,59]. For reflectance, approximately 1 mm thick uniform layer of samples is placed metal cups for measurements. Bi-conical reflectance measurements were performed by means of a Bruker A513 accessory. The reflectance standard is a gold-coated sandpaper for measurements along the entire 1 to 100 μm . The standard spectral resolution is 4 cm^{-1} , and the spot size is 48 mm for emissivity measurements. The spectral range of our analysis is from 0.5 to 16 μm , namely the infrared spectrum (IR) from Visible-Near (VNIR) to Thermal (TIR). The reflectance spectra of all samples are measured at room temperature (RT) and 193 K, and these are frozen by means of a FRIKA cold box B 35–85.

2.3. Emissivity and Reflectance Data Reduction

The collected emissivity and reflectance spectra were reduced to clean them from instrumental features. The background was removed by a linear interpolation between the estimated points on the two sides of a maximum, and a straight line has been drawn between the edges for each band. The band depth is determined using the equation $D = (R_c - R_b)/R_c$. The area was computed by a simple integration. The width has been computed by intersecting the continuum-removed band with a horizontal line passing through half depth. More information on the reduction of emissivity and reflectance data can be found in the work of Comodi et al. [38].

2.4. X-ray Diffraction Measurements and Rietveld Analysis

X-ray powder diffraction measurements were made with a Philips PW 1830 diffractometer (Koninklijke Philips N.V., Amsterdam, The Netherlands), with a graphite monochromator and using the $\text{CuK}\alpha$ radiation ($\lambda = 1.54184 \text{ \AA}$). Data were taken with a step scan of 0.02 $^\circ$ /step and a step time of 100 s/step.

Quantitative measurements of the collected data were carried out by means of the Rietveld refinement method [60], as implemented in the EXP-GUI GSAS software (Windows version 2001, University of California, Berkeley, CA, USA) [61,62]. The starting crystal structure data were selected from the *American Mineralogist* Crystal Structure Database [63]. Crystal structures were plotted using CrystalMaker software (Software version 10.6, CrystalMaker Software Limited, Oxford, UK) [64]. We used scattering factors for neutral atoms. The refined parameters were background, fitted with a 17 to 28-term Chebyshev polynomial function, profile functions of pseudo-Voigt type, scale factor, instrument zero point, and the crystal lattice constants. When needed, we applied the March–Dollase formulation for preferred orientation [65] correction.

3. Results

The emissivity and reflectance spectra collected at different temperatures are reported subsequently for each sample. Table 2 reports the position and assignation of the observed bands of the reflectance spectra, which was collected at 298 K. The data collected at 603 K together with the temperature dependence of the bands parameters, full width at half maximum (FWHM) and depth, considering that the evolution with temperature is generally linear [18], for emissivity data are in Supplementary Table S1.

For hydrous samples, in agreement with literature data e.g., [18,66], the H_2O and OH absorption fundamental and combination bands were considered. In the spectra collected at low temperature, additional peaks related to the ice formation in the sample chamber are evident at approximately 1.4 μm and 1.9 μm . For all the samples, the common features

related to the CO_3^{2-} group were also observed. Common features of the studied anhydrous carbonates (natrite, shortite, and nyerereite) are the presence of absorption bands in the 11.24–6.66 μm (889–1500 cm^{-1}) range corresponding to fundamental vibrational modes of CO_3^{2-} . In addition, a prominent band around 5.68 μm (1760 cm^{-1}) is present in almost all the studied samples due to either the structural water in hydrated samples or the hygroscopic water in anhydrous samples. Some anhydrous carbonates show H_2O bands, even if H_2O is not part of the mineral structure (indicated as H_2O^+), which is probably due to a small amount of hygroscopic H_2O trapped at grain boundaries. The comparison of emissivity spectra collected at different temperatures for each sample are reported, using the same scale to highlight linear and nonlinear changes. The temperature usually increases the deepening of most absorption bands, whereas it does not affect the band position. The low temperature reflectance spectra display more detailed and define absorption bands. The temperature range is not low enough to estimate the presence of additional bands and evaluate some bands parameters trends such as the decreasing temperature. For some modes, nonlinear changes were observed with temperature, indicating that either dehydration or phase transitions occurred.

Table 2. CO_3^{2-} , H_2O , and OH band positions in the reflectance spectra collected at 298K for all the investigated samples. Absorption band assignments were made following De Angelis et al. [18] (a,c), Frost and Palmer [49], Clark [50], Zhu et al. [51], Adler and Kerr [66] (b), and Harner and Gilmore [40] (d). The symbols + and – indicate bands assigned to structural water (H_2O^+) and hygroscopic water (H_2O^-); see text for details.

Mineral Name	CO_3^{2-} Fundamentals (μm)				CO_3^{2-} Overtones and Combinations (μm)					OH Bands (μm)	H_2O Bands (μm)
	ν_1	ν_2	ν_3	ν_4	$2\nu_3$	$2\nu_1 + 2\nu_3$	$\nu_1 + \nu_3$	$3\nu_3$	$\nu_1 + 2\nu_3$		
Natrite ^a Na_2CO_3	9.36	11.29	6.24	14.25	3.35	1.94/ H_2O	3.86	2.34	2.54	1.52 [–]	2.88 [–]
	9.68	11.75	7.07	14.41	3.51	2.05	4.01			1.74 [–]	5.62 [–]
	9.90	12.78	7.16							1.94 [–]	5.91 [–]
Nyerereite $\text{Na}_2\text{Ca}(\text{CO}_3)_2$			6.61								2.90 [–]
		11.24	6.70	13.83	3.35	1.95/ H_2O	3.85		2.46	1.57 [–]	5.55 [–]
	9.33	11.55	6.85	14.78	3.43	2.06	3.95	2.31	2.51	1.80 [–]	5.70 [–]
		11.84	7.04				4.04			1.95 [–]	6.19 [–]
Shortite ^b $\text{Na}_2\text{Ca}_2(\text{CO}_3)_3$		11.43	6.15	13.68							
		11.71	6.93	13.90	3.41		3.80	2.31		1.72 [–]	3.02 [–]
	9.33	12.10	7.01	14.10	3.50	1.91/ H_2O	3.95	2.35	2.51	1.76 [–]	3.12 [–]
		12.47	7.13	14.36			4.06			1.91 [–]	5.51 [–]
Thermonatrite ^c $\text{Na}_2\text{CO}_3 \cdot \text{H}_2\text{O}$			6.40	14.44						1.52 ⁺	2.83 [–]
	9.57	11.31	7.04	14.97		2.04	4.05	2.22	2.44	1.74 ⁺	3 [–]
							4.42			1.94 ⁺	5.68 [–]
Trona ^d $\text{Na}_3(\text{CO}_3)(\text{HCO}_3) \cdot 2(\text{H}_2\text{O})$			6.44	14.33						1.52 ⁺	~3 [–]
	9.53		7.05	14.97		2.04		2.21		1.74 ⁺	5.61 ⁺
								2.39		1.94 ⁺	

3.1. Natrite Na_2CO_3

Natrite at room temperature is monoclinic with a space group $C2/m$ and density of 2.54 g/cm^3 [67]. The mean structure of natrite can be described globally by layers of 9-coordinated Na cationic sites (Na3) and CO_3^{2-} ions (Figure 1a). Additional Na octahedral sites (Na1,2) are found in pseudo-hexagonal channels [68]. The face that shares the Na1,2 octahedra forms a column, which is connected by triangles of CO_3^{2-} [69]. Sodium carbonate has four phase transitions (α , β , γ , δ) in the T range from 170 up to 800K [68]. The γ - Na_2CO_3 is stable below 605 K and refined as an incommensurately modulated structure [70]. Two temperature-dependence phase transitions are detected at HT: β - Na_2CO_3 at 628K and α - Na_2CO_3 at 757 K [68,69,71] (Figure 2d). The cell parameters and symmetry of natrite polymorphs are reported in Table 3. Details on the spectral behavior after phase transitions are reported in Section 4.

Table 3. Sodium carbonate (Na_2CO_3) phase transitions in the temperature range investigated. Crystallographic data are taken from Dusek et al. [68], Arakcheeva et al. [69], Arakcheeva et al. [70], Swainson et al. [71]. T (K) are phases stability temperatures ranges.

Phase	T (K)	Symmetry	Cell Parameters (Å)
α	757–1000	Hexagonal $P6_3/mmm$	$a = 5.209(2)$, $c = 6.454\text{--}6.676$
β	628–757	Monoclinic $C2/m$	$a = 9.00(2)$, $b = 5.23(2)$, $c = 6.21\text{--}6.44$, $\beta = 101.87$ (8)
γ	170–628	Monoclinic $C2/m$	$a = 8.920(7)$, $b = 5.245(5)$, $c = 6.050(5)$, $\beta = 101.35$ (8)
δ	≤ 170	Monoclinic $P2_1/n$	$a = 8.898$ (7), $b = 5.237$ (5), $c = 5.996$ (5), $\beta = 101.87$ (8)

The reflectance spectra (1 to 5 μm) (Figure 2a) show very weak CO_3^{2-} absorption features due to overtones and combinations at 2.05, 2.34, 2.54, 3.35, 3.51, 3.86, and 4.01 μm . In the spectral range from 5 to 16 μm (Figure 2b), the bands are less deep and defined, and they are generated by fundamental vibrational modes of CO_3^{2-} . The absorption features at 6.24, 7.07, and 7.16 μm are assigned to $\nu_3(\text{CO}_3^{2-})$ vibrational modes. The $\nu_2(\text{CO}_3^{2-})$ fundamental modes generate the peaks at 11.29, 11.75, and 12.78 μm . The last part of the natrite reflectance spectra is characterized by the presence of one evident absorption band at 14.25 μm generated by ν_4 vibrational modes. The emissivity spectra (Figure 2c) exhibit CO_3^{2-} ν_4 and ν_2 modes at 681 and 796 cm^{-1} . The overlapping of several overtones/combinations and fundamental vibrational modes of CO_3^{2-} generates the features centered at 1178 and 1487 cm^{-1} . The well-defined bands at 2068, 2243, and 2657 cm^{-1} are due to overtone and the combination of carbonates group relative to $\nu_1 + \nu_3$ and $2\nu_3$. The absorbed water molecules cause peaks at 1764, 2974, and 3215 cm^{-1} . The shifts in the centers of the absorption bands and the variation in their shape in the spectra collected at $T = 603$ K are caused by phase transitions ($\gamma\text{-Na}_2\text{CO}_3 \rightarrow \beta\text{-Na}_2\text{CO}_3$; $\beta\text{-Na}_2\text{CO}_3 \rightarrow \alpha\text{-Na}_2\text{CO}_3$), as reported by Harris and Salje [43] (Figure 2d).

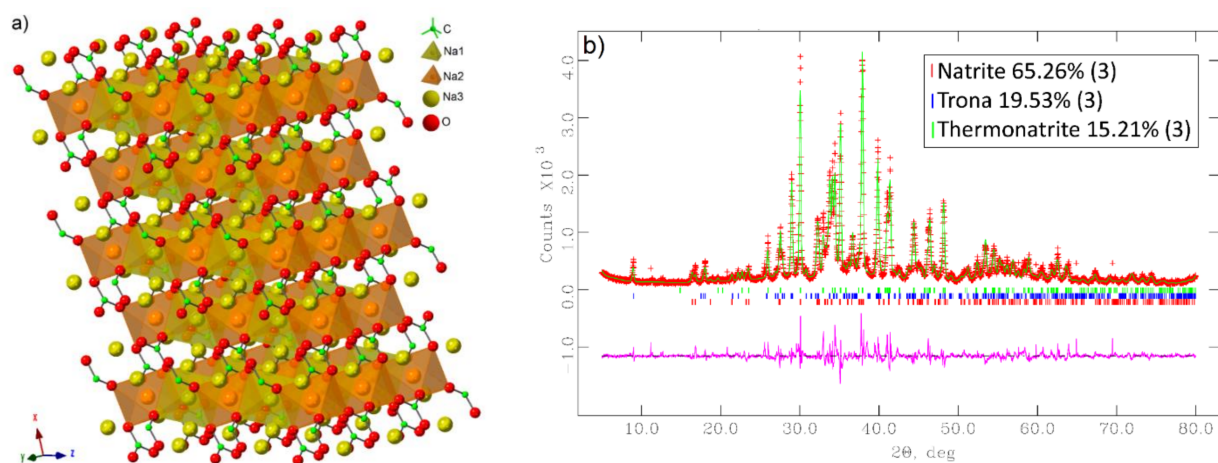


Figure 1. (a) Crystal structure of natrite [67]. The sticks represent the C ... O bonds. (b) The X-ray diffraction pattern of the sample defined as natrite collected at room temperature and refined by the Rietveld method [60] with final Rp parameter = 0.099.

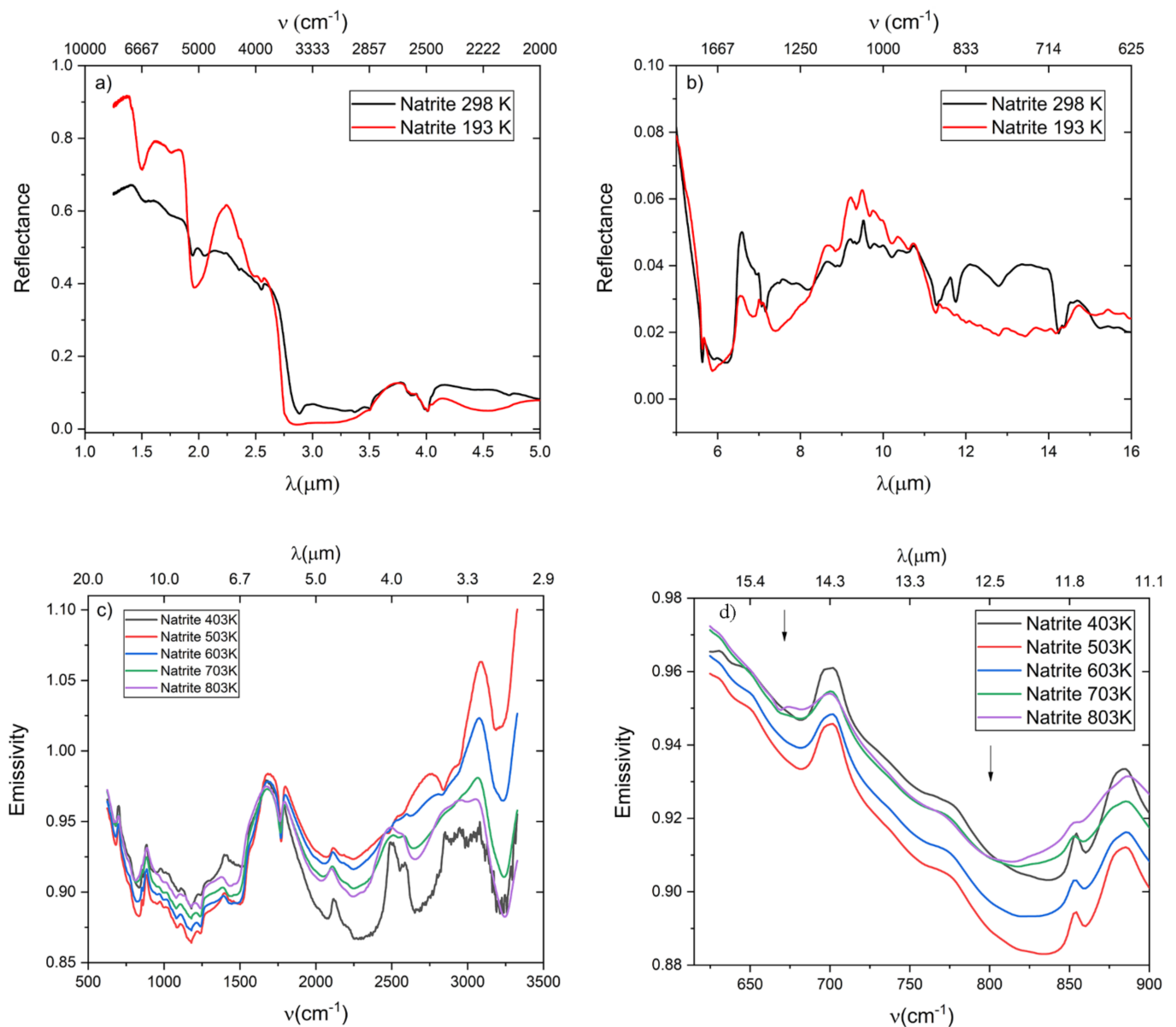


Figure 2. Reflectance spectra at room temperature and 193 K (a,b) and emissivity measurements from 403 to 803 K (c) of natrite. Focus on the absorption bands centered at ≈ 669 and ≈ 794 cm^{-1} (denoted by arrows) for the emissivity spectra of sample defined natrite Na_2CO_3 (d).

3.2. Nyerereite $\text{Na}_2\text{Ca}(\text{CO}_3)_2$

Synthetic nyerereite has a three-component orthorhombic twinned structure with either $Pbca$ or $P2_1ca$ space groups [72,73] and density 2.54 g/cm^3 [72]. The unit cell of nyerereite is $a = 10.0713(5)$ \AA , $b = 8.7220(2)$ \AA , and $c = 12.2460(4)$ \AA [72]. The framework of $\text{Na}_2\text{Ca}(\text{CO}_3)_2$ can be described as a stacking of close-packed Na- and Ca-layers in a six-layered close-packed structure, the layers orientation is (001) [72] (Figure 3a).

The reflectance spectra of nyerereite show evident peaks in the first part of the spectra (Figure 4a). We identify overtone and combination CO_3^{2-} bands located at 2.31 ($3\nu_3$), 2.46, and 2.51 μm ($\nu_1 + 2\nu_3$). Diagnostic overtones and combinations are present at 3.35 and 3.43 μm due to $2\nu_3(\text{CO}_3^{2-})$, whereas absorption features at 3.85, 3.95, and 4.04 μm are due to $\nu_1 + \nu_3(\text{CO}_3^{2-})$ vibrational modes. In the last part of the spectra (Figure 4b), we detect fundamental absorption features situated near 6, 9, 12, and 14 μm due to ν_3 , ν_1 , ν_2 , and ν_4 CO_3^{2-} vibrational modes, respectively.

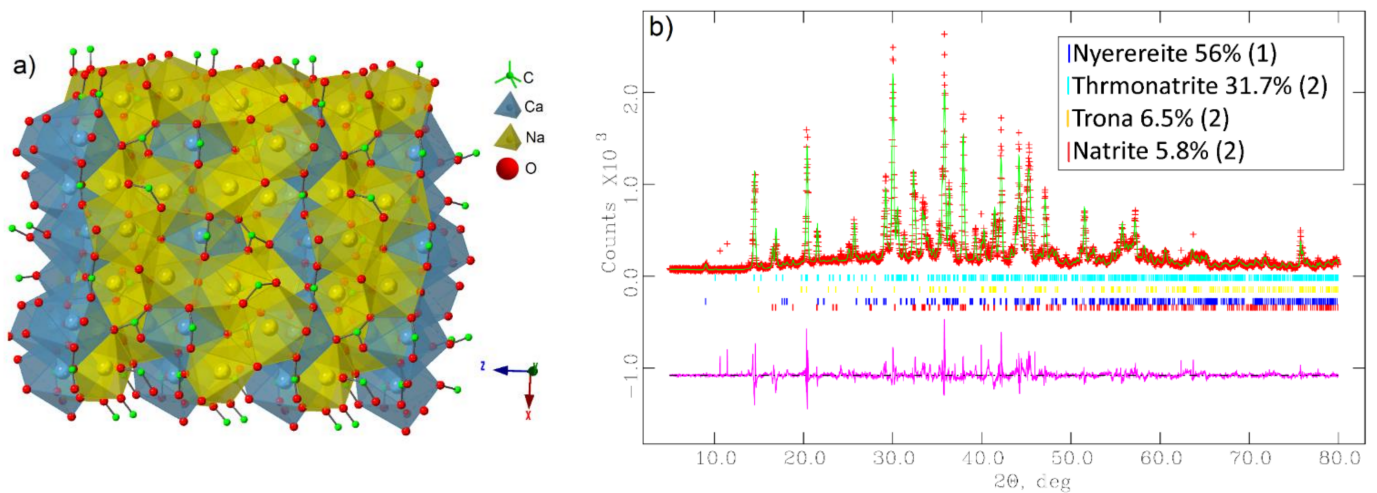


Figure 3. (a) Crystal structure of nyerereite projected along the y-axis [72]. The sticks represent the C ... O bonds. (b) X-ray diffraction pattern of the sample collected at room temperature and refined by the Rietveld method [60] with $R_p:0.09$.

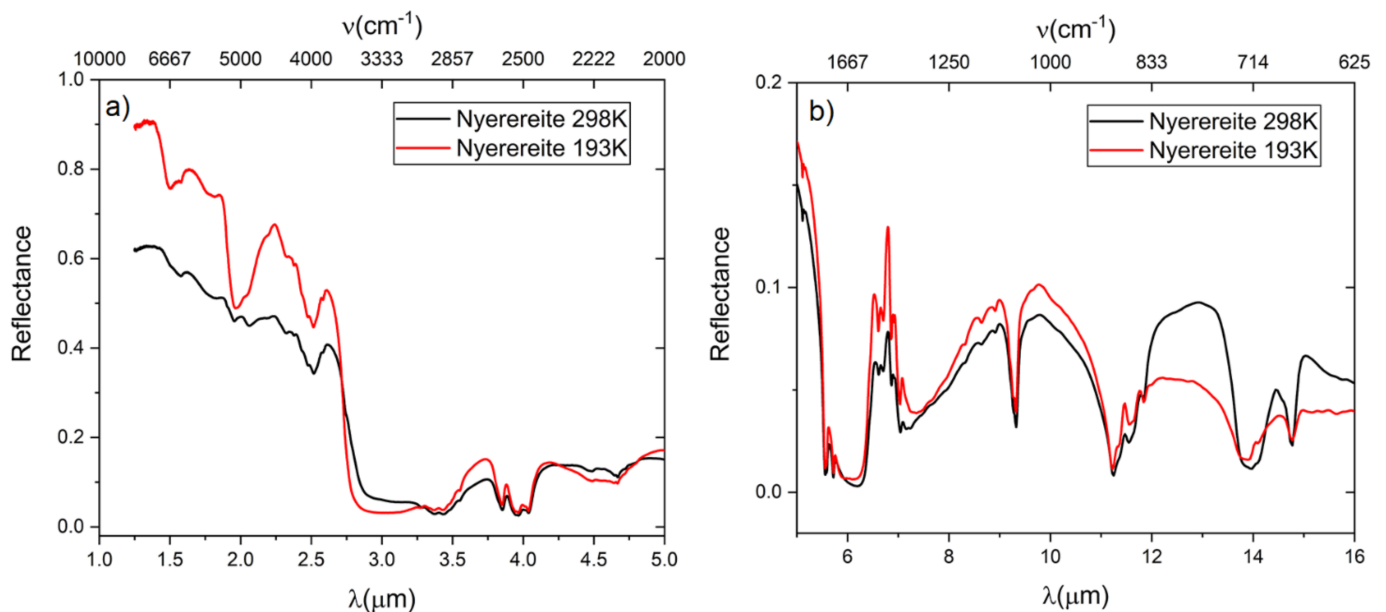


Figure 4. Reflectance spectra at room temperature and 193 K of nyerereite (a,b).

3.3. Shortite $\text{Na}_2\text{Ca}_2(\text{CO}_3)_3$

Shortite is orthorhombic with space group $Amm2$, $a = 4.947(1) \text{ \AA}$, $b = 11.032(2) \text{ \AA}$, and $c = 7.108(1) \text{ \AA}$ and a density of 2.62 g/cm^3 [74]. The structure (Figure 5a) is made by distinct layers of Na-CO_3 and $\text{Ca}_2\text{Na}(\text{CO}_3)_2$. Within the unit cell, two sodium sites (Na1 and Na2) and one Ca site are located, lying in a disordered trigonal prismatic site, seven-fold site, and nine-fold site, respectively [27]. Two distinct carbonate ions are present: C1, which goes out of plane with respect to the oxygens of approximately 0.03 \AA , and C2, where carbonate is symmetry constrained to be flat [27]. As both C1 and C2 are approximately aligned with their edges along the Ca site at a regular interval [27], the Ca site achieves a nine-fold coordination.

The reflectance spectra of shortite are characterized by well-defined absorption bands in the range from 1 to 5 \mu m (Figure 6a) with features at 2.31 ($3\nu_3$), 2.35 ($3\nu_3$), and 2.51 ($\nu_2 + \nu_3$) \mu m due to the overtone and combination bands of the CO_3^{2-} group. These modes generate diagnostic and interesting features at 3.41 and 3.50 \mu m caused by $2\nu_3$ (CO_3^{2-}), and at 3.80 , 3.95 , and 4.06 \mu m assigned to $\nu_1 + \nu_2$ (CO_3^{2-}). Fundamental vibrational modes are present in the spectral range over 6 \mu m (Figure 6b). From 6 to 7.5 \mu m , the bands are due to $\nu_3(\text{CO}_3^{2-})$; whereas in the range from 11 to 12.5 \mu m , the absorption features are ascribed to $\nu_2(\text{CO}_3^{2-})$ vibrational modes. The two bands at 13.68 and 14.36 \mu m are generated by $\nu_4(\text{CO}_3^{2-})$ mode. The emissivity spectra (Figure 6c) show defined peaks at 1226 and 1486 cm^{-1} due to the ν_3 fundamental vibrational modes of the CO_3^{2-} . The overtones and combinations of this group are detected at 2067 , 2283 , 2604 , and 2699 cm^{-1} . In this sample, the absorption features ν_4 modes are detected at 831 cm^{-1} and there are no emissivity spectra above 403K due to its dissolution after this temperature.

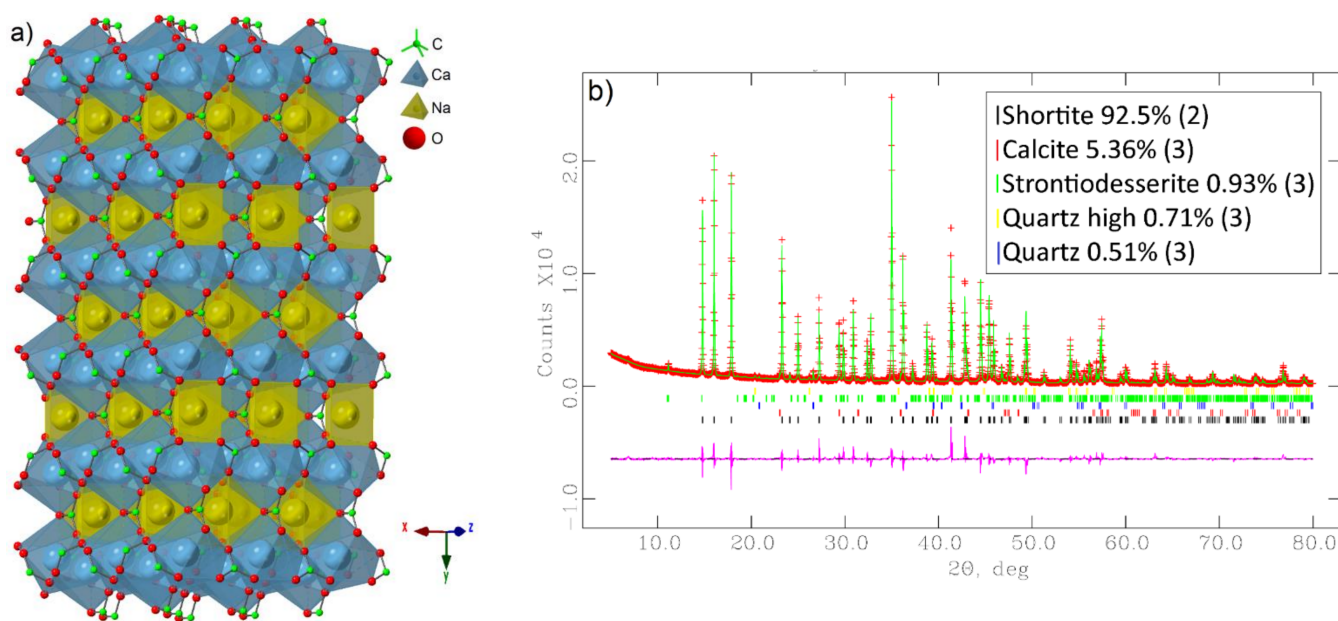


Figure 5. (a) Crystal structure of shortite [74]. The sticks represent the C . . . O bonds. (b) The X-ray diffraction spectrum of the sample defined as shortite collected at room temperature refined by the Rietveld method [60] with R_p . 0.064.

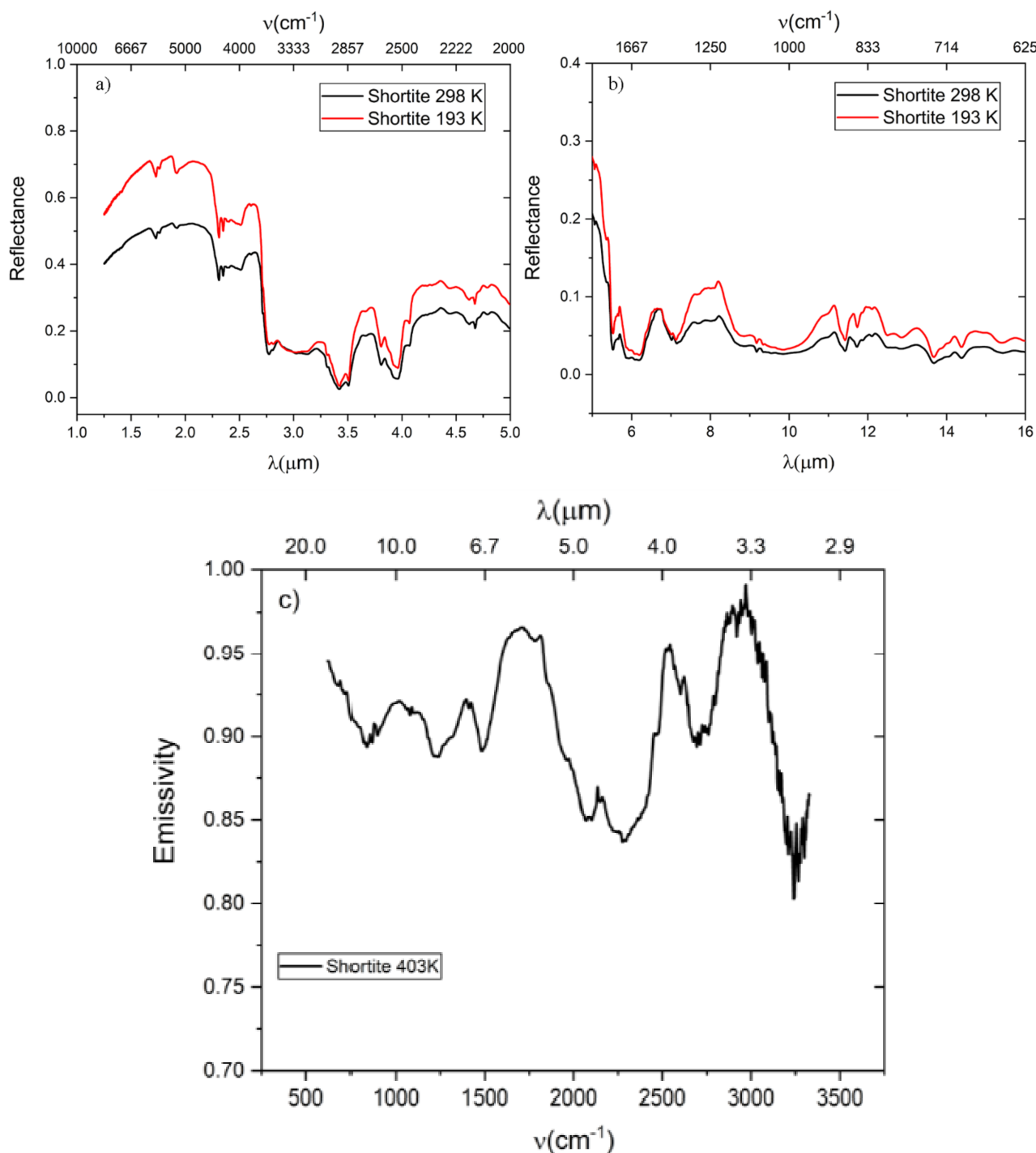


Figure 6. Reflectance spectra at room temperature and 193 K (a,b) and emissivity measurements at 403 K (c) of shortite.

3.4. Thermonatrite $\text{Na}_2\text{CO}_3 \cdot \text{H}_2\text{O}$

Thermonatrite, the sodium carbonate monohydrate, is orthorhombic with space group $P2_1ab$, unit cell parameters $a = 6.472(2) \text{ \AA}$, $b = 10.724(3) \text{ \AA}$, $c = 5.259(2) \text{ \AA}$ [75], and density of 2.25 g/cm^3 [76]. The CO_3^{2-} groups within the thermonatrite crystal structure have planes almost perpendicular to the a -axis forming sheets that are stacked in columns along the same axes (Figure 7a). Two adjacent CO_3^{2-} groups within the same column are both ionically bonded to four Na ions and hydrogen bonded by a water molecule; whereas adjacent CO_3^{2-} molecules in the same sheet are linked by the Na

ions that lie above and below the sheet [75] (Figure 8a). The H₂O molecule is lost in the temperature range between 360 and 363K; over these temperatures, only sodium carbonate occurs [77].

The reflectance spectra of thermonatrite (Figure 8a,b) are characterized by the presence of poorly marked absorption features due to the presence of water that overlaps the bands of the CO₃²⁻ group. In the first part of the spectra (1–5 μm), the absorption features of CO₃²⁻, caused by overtone and a combination at 2.04 (2ν₁ + 2ν₃), 2.22 (3ν₃), 4.05 (ν₁ + ν₃), and 4.42 (ν₁ + ν₃) μm are detected. The bands related to CO₃²⁻ fundamental vibrational modes are present at 6.40 (ν₃), 7.04 (ν₃), 9.57 (ν₁), 11.31 (ν₂), 14.44 (ν₄), and 14.97 (ν₄) μm. The emissivity spectrum (Figure 8c) is closely related to the natrite mineral. In fact, ν₄ and ν₂ bands are present at 651 and 790 cm⁻¹. The band centered at 1117 cm⁻¹ is made by the overlap of several CO₃²⁻ overtone and combination features. Other absorption bands related to overtone and combination are located at 2013, 2245, and 2677 cm⁻¹ due to ν₁ + ν₃/2ν₃ (CO₃²⁻). The presence of water molecule generates absorption features at 1768 and 3241 cm⁻¹. As reported in the natrite sample, the bands shifting and changing shape in the emissivity spectra collected at 703 and 803 K are related to phase transition from γ- to β-Na₂CO₃ and β- to α-Na₂CO₃ (Figure 8d). In the thermonatrite sample, the variations of the fundamental vibrational modes during heating are much more evident than in the natrite sample.

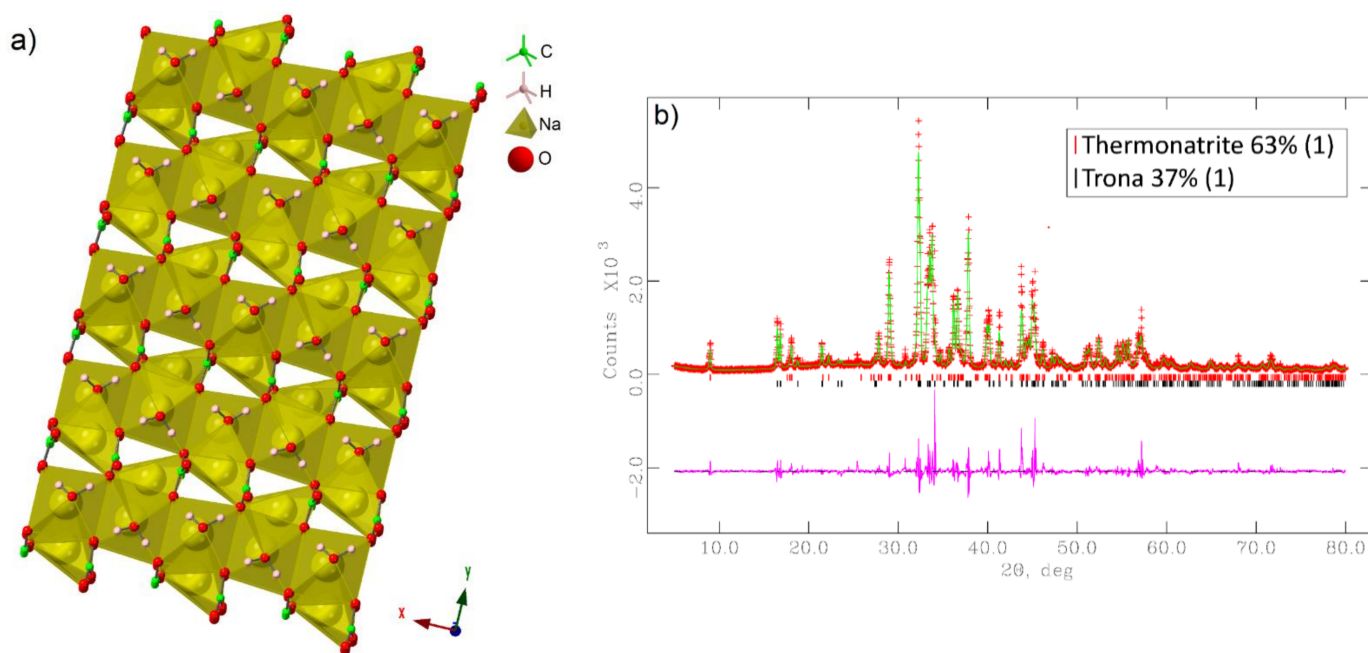


Figure 7. (a) Crystal structure of thermonatrite projected along the z-axis [75]. The sticks represent the C . . . O bonds and OH . . . O hydrogen bonds. (b) X-ray diffraction profile of the sample define as thermonatrite collected at room temperature and refined by the Rietveld method [60] with Rp. 0.10.

3.5. Trona Na₃(CO₃)(HCO₃)·2(H₂O)

Trona is an interesting mineral that contains the unusual combination of both a carbonate and bicarbonate anion [78] (Figure 9a). It crystallizes in the monoclinic space group C2/c with cell parameters $a = 20.41(3)$ Å, $b = 3.49(1)$ Å, $c = 10.31(1)$ Å, $\beta = 106.2(1)^\circ$ [79], and density 2.13 g/cm³ [80]. The crystal structure of the minerals is characterized by units of three edge-sharing sodium polyhedra cross-linked by carbonate groups and hydrogen bonds [78]. Thus, each Na ion is surrounded by six O atoms, some belonging to the carbonate ion and some belonging to the water molecule. Two different Na sites are present, being the one octahedrally coordinated and the other one at the center of a slightly distorted

trigonal prism [78]. The CO_3^{2-} group has one oxygen bonded by a hydrogen bridge to an oxygen of another carbonate ion, forming what has been usually called a complex $[\text{HC}_2\text{O}_6]^{3-}$ anion. The disordering of H in the $[\text{HC}_2\text{O}_6]^{3-}$ complex gives rise to the sharing of one H between the carbonate units, thus producing the mixed carbonate/bicarbonate character of these anion groups [79].

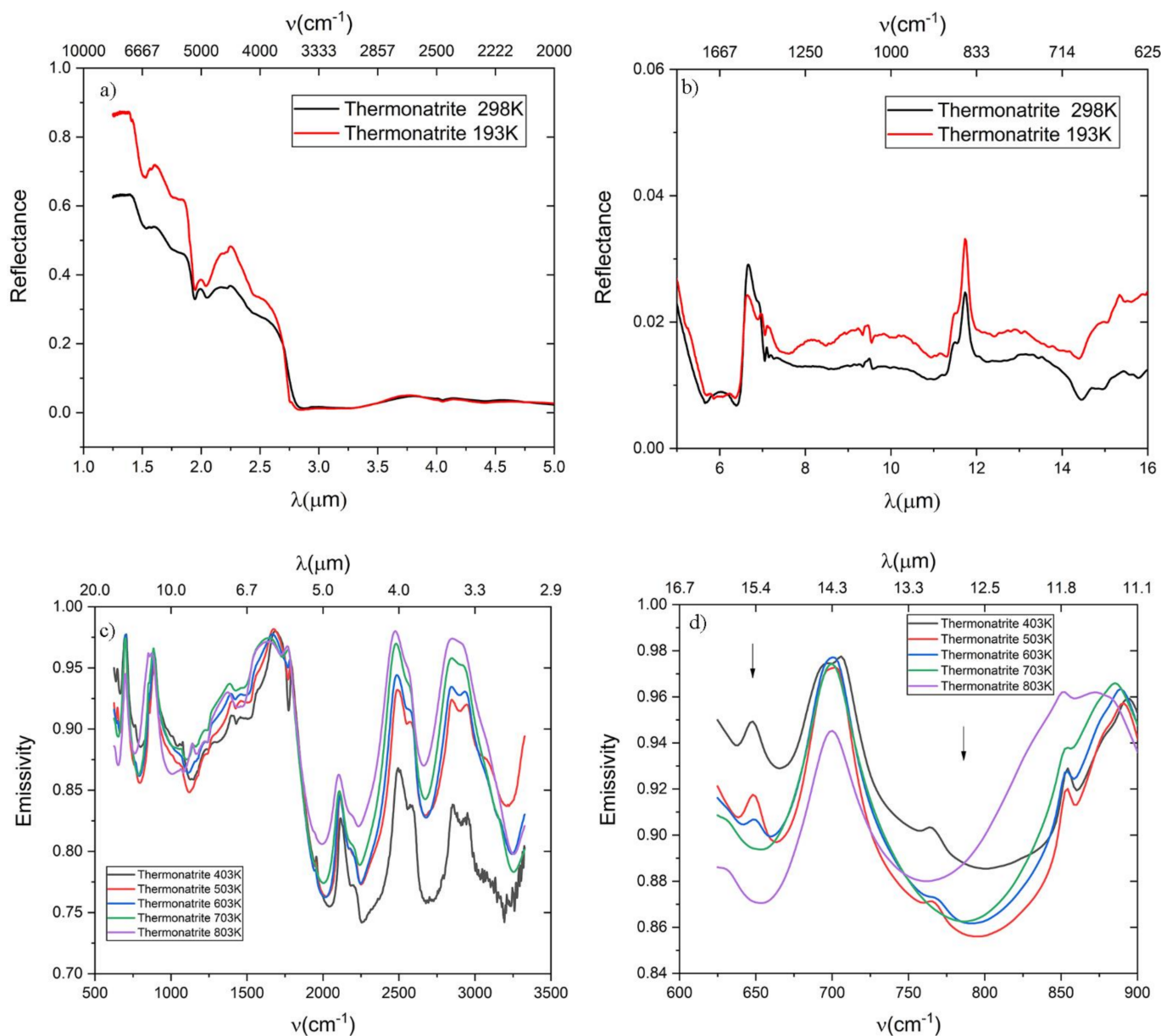


Figure 8. Reflectance spectra at room temperature and 193 K (a,b) and emissivity measurements from 403 to 803 K (c) of thermonatrite. (d) Focus on the absorption bands centered at ≈ 669 and ≈ 794 cm^{-1} (denoted by arrows) for the emissivity spectra of sample defined thermonatrite $\text{Na}_2\text{CO}_3 \cdot \text{H}_2\text{O}$.

The reflectance spectra of trona (Figure 10a,b) have poorly marked or absent bands due to the presence of water molecules (15.94 wt %). We observed evident and typical H_2O absorption features at 1.52, 1.94, and 5.61 μm . CO_3^{2-} overtone and combination vibrational modes are detected at 2.04 ($2\nu_1 + \nu_3$), 2.21 ($3\nu_3$), and 2.39 ($3\nu_3$) μm . Absorption bands at 6.44 (ν_3), 7.05 (ν_3), and 9.53 (ν_1) μm are due to fundamental vibrational modes of CO_3^{2-} . The emissivity spectra (Figure 10c) are strictly related to natrite and thermonatrite samples, as they are subject to the same phase transitions at the investigated temperature. In this

case, we do not have a split peak before phase transitions. In fact, the absorption features present at 660 and 791 cm^{-1} are due to the fundamental CO_3^{2-} vibrational modes ν_1 and ν_4 , respectively, and the bands position at high temperature probably shift due to phase transitions (Figure 10d). The overtone and combination of this group ($\nu_1 + \nu_3$ and $2\nu_3$) generate the bands at 2001 , 2244 , and 2670 cm^{-1} . Water in trona shows two bands at 1768 and 3238 cm^{-1} . Trona decomposes in two steps, in relation of water loss between 373 and 407 K [81], generating sodium carbonate as confirmed by XRPD data collected after the eating process (Figure 11).

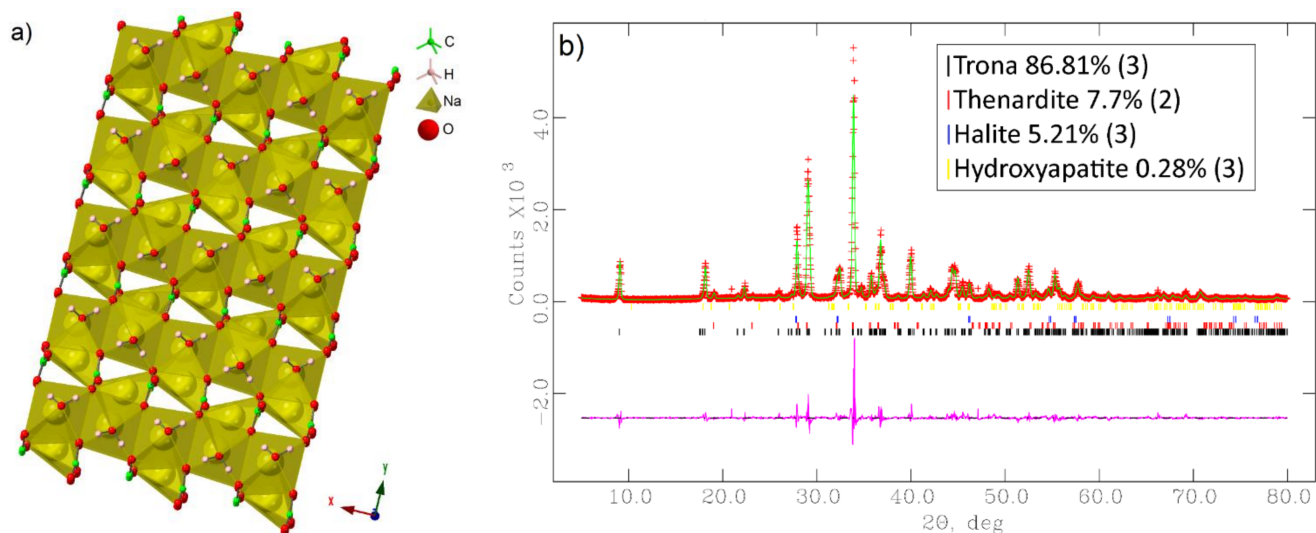


Figure 9. (a) Crystal structure of trona projected along the y-axis [79]. The sticks represent the C ... O bonds and OH ... O hydrogen bonds. (b) X-ray diffraction profile of the sample define as trona collected at room temperature and refined by the Rietveld method [60] with Rp. 0.11.

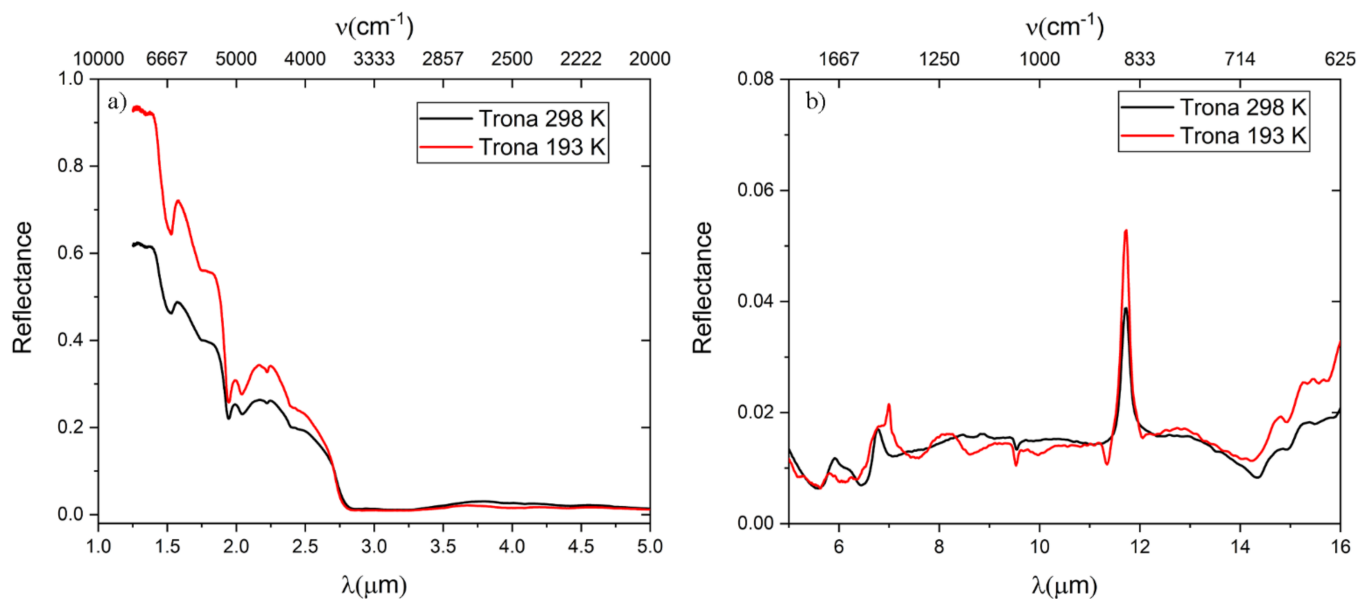


Figure 10. Cont.

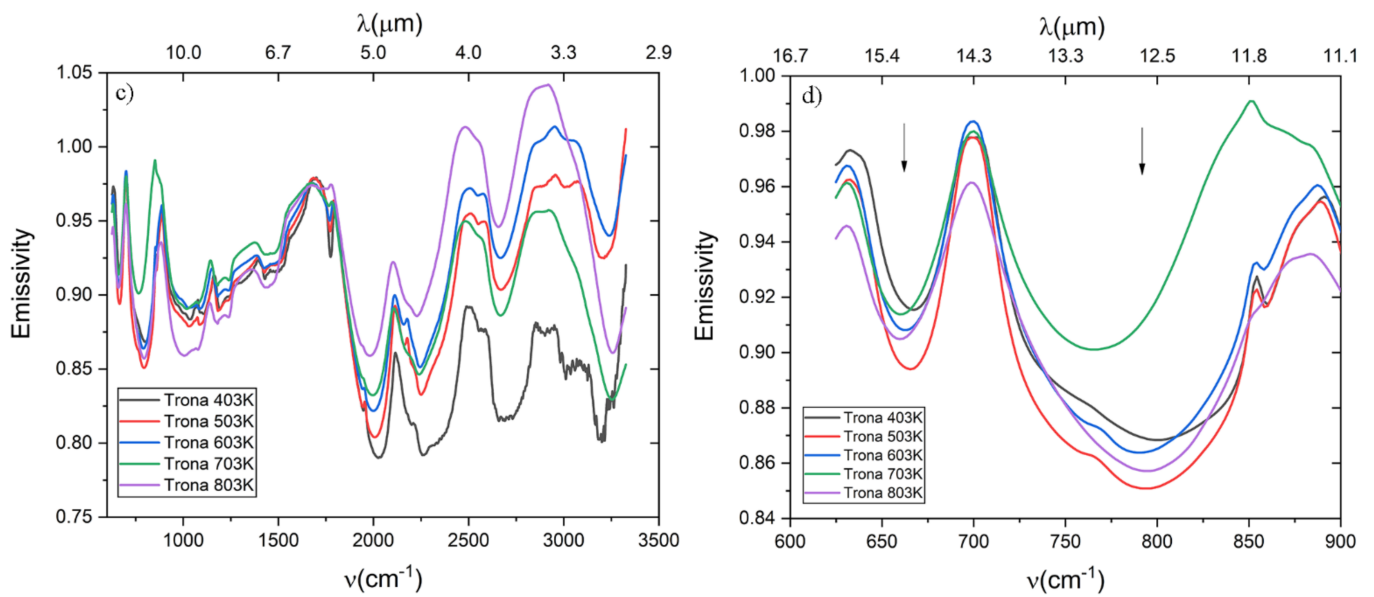


Figure 10. Reflectance spectra at room temperature and 193 K (a,b) and emissivity measurements from 403 to 803 K (c) of trona. Focus on the absorption bands centered at ≈ 669 and ≈ 794 cm^{-1} (denoted by arrows) for the emissivity spectra of the sample defined trona $\text{Na}_3(\text{CO}_3)(\text{HCO}_3) \cdot 2(\text{H}_2\text{O})$ (d).

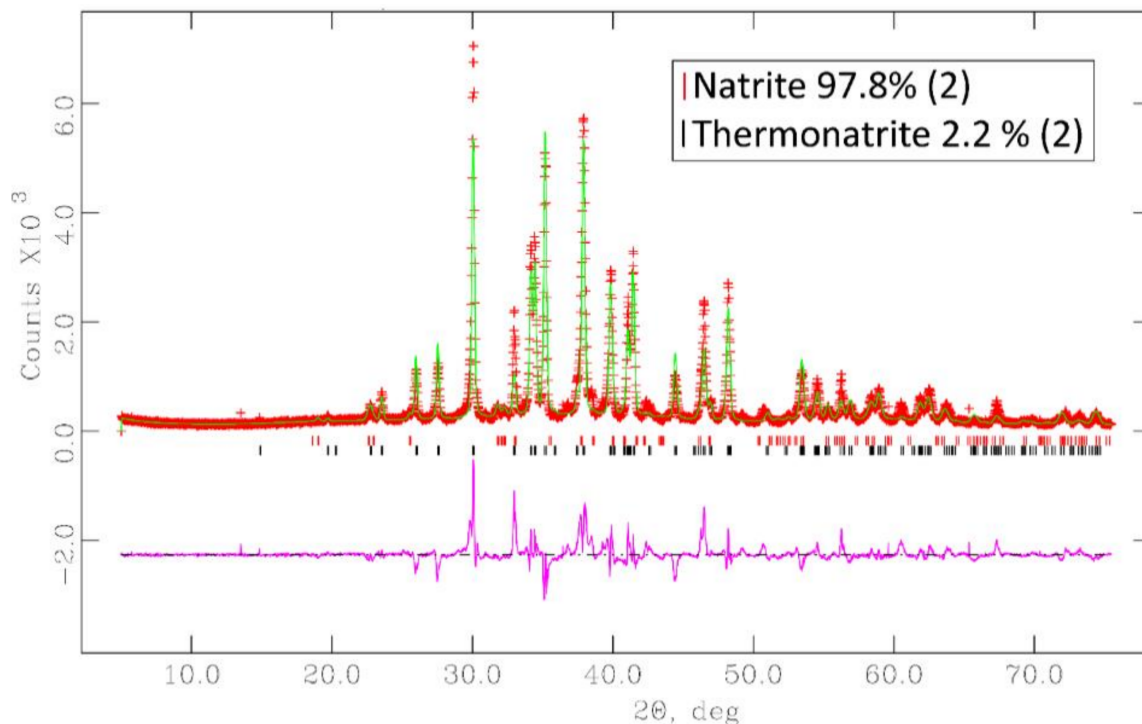


Figure 11. Room temperature X-ray powder diffraction pattern of trona after heating, refined by the Rietveld method [60] with R_p 0.15.

4. Discussion

In the reflectance spectra, the absorption bands near 3.4 and 3.9 μm are considered diagnostic for the detection and selection of carbonate minerals [18,82]. The anhydrous samples examined in this paper show distinct and well-defined bands in the above-mentioned ranges. Comparing the spectra of the shortite, nyerereite, and natrite samples (Figure 12a), a variation of the band positions in relation to the change of the Ca:Na ratio is shown, all considering that: in $\text{Na}_2\text{Ca}_2(\text{CO}_3)_3$ -shortite, the Ca:Na ratio is 2:2; in $\text{Na}_2\text{Ca}(\text{CO}_3)_2$ -nyerereite, Ca:Na = 1:2, and in Na_2CO_3 -natrite, Ca:Na = 1:0. The plot (Figure 12b,c) shows that decreasing the Ca:Na ratio, the 3.4 and 3.9 μm bands shift toward shorter wavelengths. Thus, the variation in Na:Ca concentration influences the position of the bands area that decreases as the ratio increases.

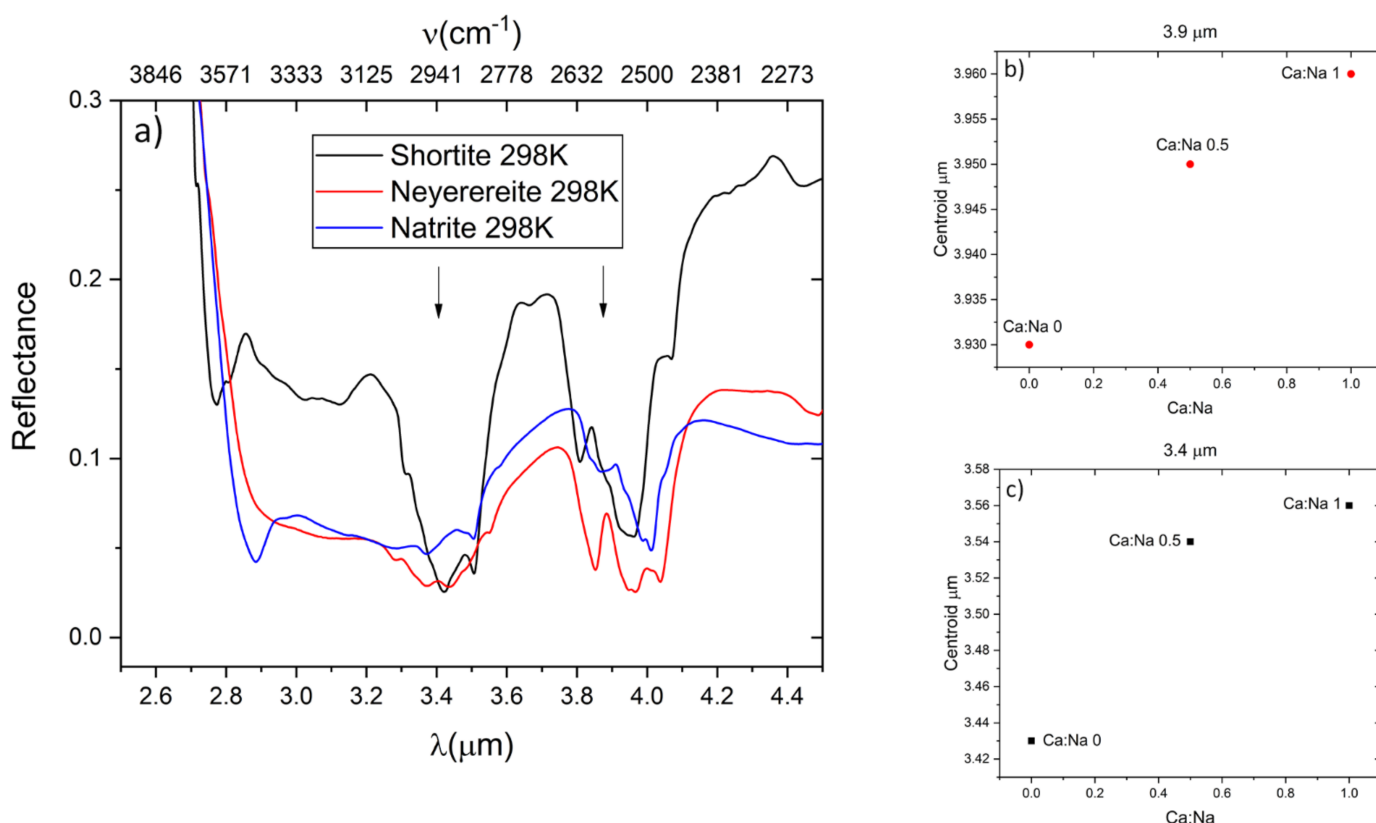


Figure 12. Comparison of 3.4 and 3.9 μm bands (underlined by arrows) for shortite, nyerereite, and natrite minerals in relation to the different Na:Ca ratio (a). The centroid variation is reported in (b) and (c).

Moreover, the bands located at 3.9 μm show an additional interesting behavior depending on the carbonate mineral structure and chemistry. In fact, the simple salts such as Na_2CO_3 -natrite are characterized by an uncomplete split broad band. On the other hand, double carbonates such as $\text{Na}_2\text{Ca}_2(\text{CO}_3)_2$ -shortite and $\text{Na}_2\text{Ca}(\text{CO}_3)_2$ -nyerereite show well-defined doublet peaks at 3.9 μm (Figure 13). Features at 3.4 and 3.9 μm are due to C-O stretching frequencies [83]. In double carbonates, some C-O bonds are shared between two cations (in the shortite Na^+ and Ca^{2+}), and these can generate a different arrangement of the cations in the crystal structure. In this configuration, the CO_3^{2-} group in double carbonate shares an oxygen atom with two different cations, than it is possible to conclude that when carbonate groups are distorted by regular planar symmetry, this mode splits into two components [84].

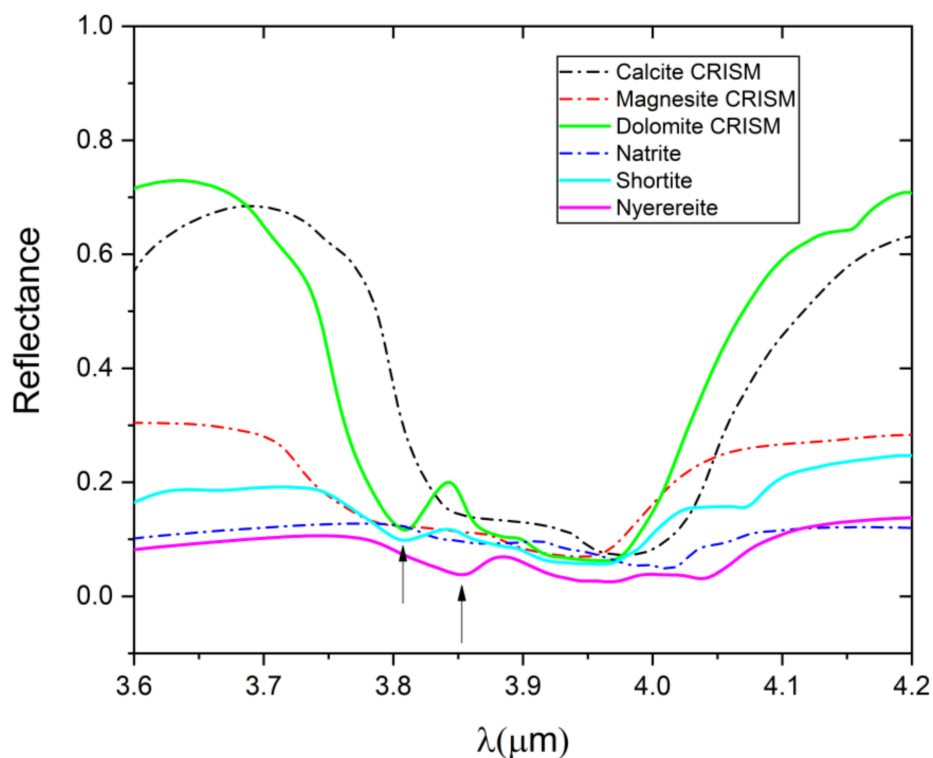


Figure 13. Reflectance spectra of single and double carbonates calcite CaCO_3 (LACB09A), magnesite MgCO_3 (KACB06A), dolomite $\text{CaMg}(\text{CO}_3)_2$ (F1CC05B), natrite Na_2CO_3 , nyerereite $\text{Na}_2\text{Ca}(\text{CO}_3)_2$, and shortite $\text{Na}_2\text{Ca}_2(\text{CO}_3)_3$. Focus on the absorption bands at $\approx 3.8 \mu\text{m}$ due to C-O vibrational modes underlined by arrows. The dashed line highlights the evident peak splitting in the double carbonates. Spectral numbers refer to samples in the CRISM spectral library (<https://speclib.rsl.wustl.edu/> (accessed 4 June 2021)).

Among the investigated minerals, natrite, thermonatrite, and trona undergo complete de-hydration between 373 and 600 K, which determine a new phase with higher density with respect to the low-temperature ones. The increase of density can be relevant in trona, where it approaches 19.2%. The density variation at high temperature is an important parameter that strongly influences geodynamics and volcanism [85]. The density change connected to phase transition could have a strong impact on the formation of free water due to the structural rearrangements, which may affect the planetological models [38].

The occurrence of possible phase transitions in sodium carbonate samples by emissivity data is well evaluated by looking at the ≈ 669 and $\approx 794 \text{ cm}^{-1}$ bands that are due to ν_4 and $\nu_2 \text{ CO}_3^{2-}$ fundamental vibrational modes, respectively, and these are the most sensitive to temperature variations. Thermonatrite and trona at 400K become natrite, Na_2CO_3 as reported in the results section. In the temperature range between 600 and 800 K, both are subject to two phase transitions ($\gamma\text{-Na}_2\text{CO}_3 \rightarrow \beta\text{-Na}_2\text{CO}_3$; $\beta\text{-Na}_2\text{CO}_3 \rightarrow \alpha\text{-Na}_2\text{CO}_3$) [68,69]. In our measurements, the ν_4 frequencies change at high temperature (above 600K) as shown in Figure 2d, Figure 8d, and Figure 10d, where the ν_4 in the $\alpha\text{-Na}_2\text{CO}_3$ shows a single band in agreement with Harris and Salje [43]. The different shapes of the absorption bands are due to small impurities within the samples because they are natural minerals.

Carbonates on the Ceres Occator Area

As reported in the introduction section, in recent years, the composition of the surface of Ceres has attracted the interest of the scientific community, and a mixture of Mg-phyllsilicates, ammoniated clays, carbonates, and salts has been proposed [86,87]. The suggest minerals on the surface also could imply the presence of water in the form of

an ancient ocean or localized brine underneath the crust [12]. The mineralogy of Ceres is largely coherent with the bulk composition of carbonaceous chondrite [88], and Na-carbonates gave good fits [9], even if the addition of Ca-carbonates (e.g., calcite) also produces equally fine results [8]. The presence of carbonate minerals on the surface of the dwarf planet Ceres was suggested taking in consideration the absorption features in the 4 μm region of telescopic spectra. Moreover, the 3.4 and 3.9 μm absorption features in the VIR spectra of Ceres confirm the presence of carbonates, and spectral models identify anhydrous sodium carbonate (e.g., Na_2CO_3) as the best candidate for Occator crater's bright material [45].

Occator is the most well-preserved large crater where all the ancient features and textures of the formation are quite intact. [89]. The bright spots on Ceres are presumed to be the results of cryovolcanism and/or post-impact hydrothermal activity [90,91]. These phenomena imply the rising of material and the interaction between the surface and the subsurface [92]. Moreover, some bright faculae were modeled using hydrated sodium carbonates minerals (thermonatrite and trona) [9]. The presence of this hydrated form, unstable at Ceres's surface condition, is strictly related to the continuous genesis of new material [12,93].

In this paper, we compare the VIR measured spectra by the Dawn mission of the Ceres Occator crater (taken from [45]) and our anhydrous samples collected at room temperature (Figure 14a). The band's positions in the 3–4 μm region of the three anhydrous samples are in good agreement with those detected on the surface spectra, without considering the band's shapes. As reported above, the band's position shifts between the samples are related to the different Na:Ca ratios. As a conclusion, on the basis of a qualitative comparison, the presence of double carbonates (Na-Ca) cannot be excluded in the Occator area. The possible occurrence of these two compounds does not imply a change in the assumptions made about the genesis of carbonates on Ceres [8], as they are minerals produced by the rock–fluid interaction, too. However, as observed in the Ca-Mg carbonate system, some important physical properties, such as solubility, are influenced by the Ca:Mg ratio in the mineral crystal structure, being quite different in calcite and in dolomite also as a function of cation disorder [94,95].

In the Na-Ca system, natrite is very soluble in water (solubility ≈ 30 g/100mL at room T), whereas calcite has a lower solubility in CO_2 free water (solubility ≈ 0.0013 g/100mL at room T). That is, double Na-Ca salts can have solubility and dissolution rates different from the end members, strongly affecting physical properties such as permeability. Discerning about the likely occurrence of Na-Ca double carbonates could be relevant to model the genetic environments of carbonates in the Occator area and in planetary bodies.

Once the qualitative comparison has been made, using an algorithm *mixture-fit*, we carried out a quantitative comparison, and we obtained the mixtures in Figure 15 to represent the surface composition of the Ceres Occator area. Details and descriptions of how the tool works can be found in Appendix A. We aimed to test if the Na carbonate minerals studied within this work, shortite and nyerereite, provide a good fit and if they can be considered as possible alternatives with respect to literature data [8,9] to represent the surface. Focusing on the phases proposed by Carrozzo et al. [8] and De Sanctis et al. [9], we modeled the spectrum of Ceres Cerealia as a mix of magnetite (dark material), illite (low-albedo material), sal-ammoniac, calcite, and Na-carbonates (natrite, termonatrite, and trona). We replace the latter with the spectra of the samples studied within this work. The spectral fit using hydrated carbonates and natrite (Figure 15b,d,e) are reported to evaluate the goodness of spectral fit made by our algorithm as a check before inserting the two proposed anhydrous phases.

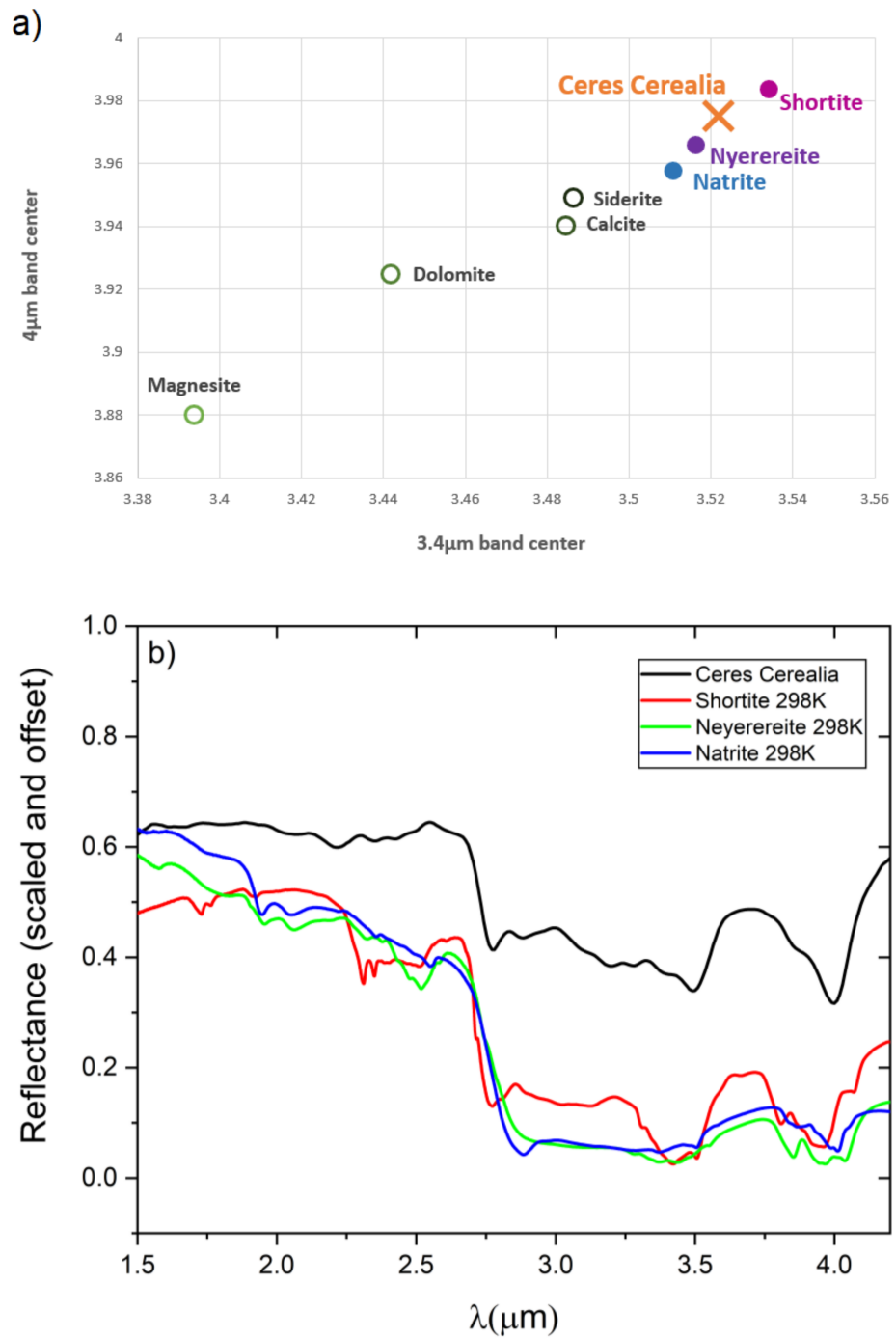


Figure 14. (a) Scatter plot of the absorption band centers for different carbonates shows that data from Ceres Cerealia bright areas are similar to those of natrite, nyerereite, and shortite, and they are quite different from other carbonates. (b) Laboratory spectra of natrite, shortite, and nyerereite at 298 K compared to spectrum of Ceres Cerealia.

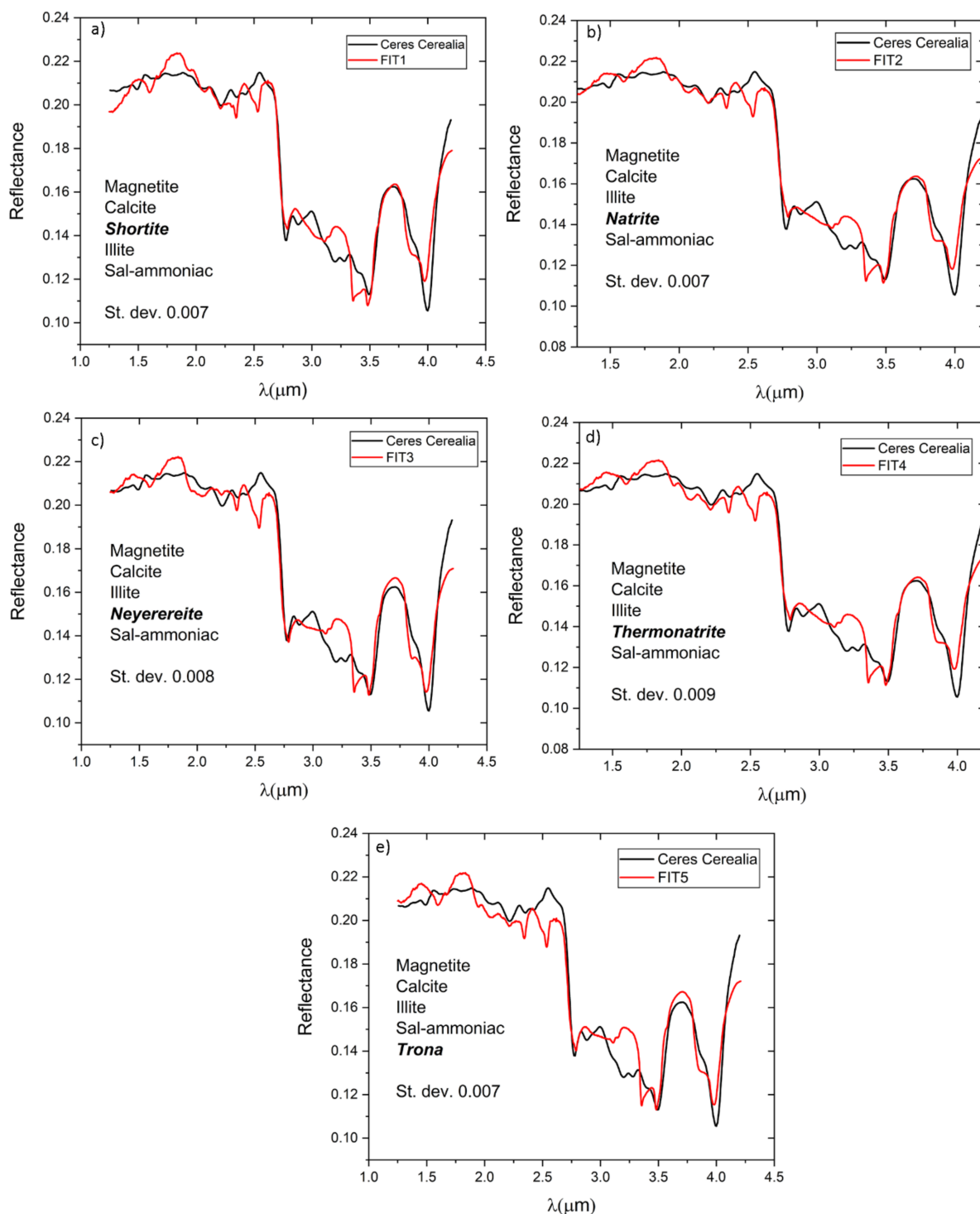


Figure 15. Results of the fitting of Ceres Cerealia (black line) spectra with different mineral mixtures by using *Mixture Fit* tool (red line): The mixtures are: (a) magnetite, calcite, shortite, illite, and sal-ammonica; (b) magnetite, calcite, illite, natrite, and sal-ammoniac; (c) magnetite, calcite, illite, neyerereite, sal-ammoniac; (d) magnetite, calcite, illite, thermonatrite, sal-ammoniac; (e) magnesite, calcite, illite, sal-ammoniac, trona. Values of the St. dev. for each mix are given in the figures. The mineral description and abundance are reported in Tables A1 and A2.

For each combination, we consider albedo constants, end-member percentages, temperatures, and effective reflectance as free parameters. On the other side, the grain size parameter is fixed in relation to the single granulometry of the data collected inside this

work. In the future, is necessary to implement within the algorithm the particle size parameters, and optical constants to obtain more realistic phase percentages and accurate fits. For these reasons, some discrepancies are evident in our fit of overtones, especially in the area near doublet bands.

The resulting mixtures show how shortite and neyerereite provide the same fine spectral fit of Na-carbonates, those made by our algorithm, as those already tested and evaluated by previous work, so we cannot exclude their presence and they could be additional good candidates to represent the surface of the Occator bright area. Given the differences in the solubility behavior of Na-Ca carbonates in water as a function of their chemical composition, the existence of the two Na-Ca carbonates may be relevant to speculate on the composition and field stability of the brines from which the surface salts are derived.

5. Conclusions

The collected data and the detailed analysis of the spectral features of CO_3^{2-} , in the different mineral species as a function of their crystal structure and cation types, give more information for the remote sensing identification of the selected phases. We focused on how the bands located at ≈ 3.4 and $3.9 \mu\text{m}$, which are essential for carbonates mineral identification, are affected by chemical composition and crystal structure, and we found a strict relation between the band's position and the Na:Ca ratio. Moreover, bands located at ≈ 3.4 and $3.9 \mu\text{m}$ could be used for giving information about the structural configuration of carbonates salts: a complete doublet of the $\approx 3.9 \mu\text{m}$ feature is present only in spectra of minerals with the metal–oxygen bond length shared between two cations.

A comparison of the $3\text{--}4 \mu\text{m}$ region spectra of the Ceres Occator area to our laboratory spectra of anhydrous Na:Ca phases suggests that the laboratory spectra have absorption features that are consistent with those seen in the Ceres Occator area. High-temperature emissivity spectra are useful to determine the dehydration conditions of hydrated Na:Ca carbonates, especially when they are either in unstable surface condition or periodically replaced by fresh material. In addition, the behavior of these salts at the temperature that can be found inside icy bodies [96,97] can constrain both the composition of the subsurface brine and/or oceans and the depth at which they release water.

The here-proposed laboratory spectra should help the future remote sensing interpretation (e.g., Juice mission with MAJIS spectro-imager) emphasizing the spectral range as more sensible to the variation due to different mineral species.

Supplementary Materials: The following are available online at <https://www.mdpi.com/article/10.3390/min11080845/s1>, Table S1: Band positions in the emissivity spectra collected at 603 K for all the investigated samples. The areas, FWHM, and depths are reported. Absorption band assignments were made following De Angelis et al. [18], Frost and Palmer [49], Clark [50], Zhu et al. [51], Adler and Kerr [65], and Harner and Gilmore [40]. Arb.u. namely arbitrary unit. The symbol for Δ FWHM/T and Δ depth/T represent the temperature dependence of FWHM and depth.

Author Contributions: Conceptualization, M.F., A.Z. and P.C.; data curation, M.F., A.Z., P.C., A.M., G.A., E.P. and R.P.; methodology, M.F., A.Z., P.C., A.M. and G.A. writing—original draft, M.F., A.Z., and P.C.; writing—review and editing, M.F., A.Z., P.C., A.M., G.A., E.P. and R.P. All authors have read and agreed to the published version of the manuscript.

Funding: This research was funded by the European Union's Horizon 2020 research and innovation programme, project number 18-EPN4-040. The experiments were partially supported by the financial program of MIUR (project no. PRIN2017-2017LMNLAW "Connect4Carbon").

Data Availability Statement: Not applicable.

Acknowledgments: We would like to thank Marco Marchesini (Eni Upstream and Technical Services) for supplying some of the analyzed samples. This research utilizes spectra acquired by Bishop, J.L. and Pieters, C.M. with the NASA RELAB facility at Brown University.

Conflicts of Interest: The authors declare no conflict of interest.

Appendix A

We reproduce Ceres Cerealia average spectrum to evaluate how to work the proposed software as an areal mixing of different end members. The *mixture-fit* tool is based on the Hapke model, which is the scattering theory most widely used to calculate synthetic reflectance spectra [45,46]. The surface of a celestial object can be a mixture of different minerals; for this reason, to compare calculate spectra with the observational data, it is necessary to create a mixture of different types of spectra. Areal mixing consists of a paragenesis of materials with different composition that are spatially isolated from one another. Areal is the most used method and the less computationally intensive, and it is the process used inside a mixture fit. The spacecraft spectra $T[j]$ can be represented as:

$$T_{[j]} = \sum_{i=1}^n w_i R_i[j].$$

In this case, n is the total number of spectra $R[j]$ to be used, and w_i represents the weight coefficient for each reference spectra, which corresponds to the abundance of the material inside the fit. The mixing model is based on the least square method [98]; the goodness of the adaptation parameter (χ^2) is studied because of the variation of the weight coefficients. The tool is based and written on Wolfram Mathematica software (licence: L5109-8903). We have developed a tool with a full graphical interface designed as an interactive easy-to-use tool for data analysis. An immediate image graphical plot presentation is included for a complete analysis. The program decodes experimental data from a text file; these format data files can be prepared with any text editor. Once uploaded inside *mixture-fit*, data can be divided in four different types: minerals including the text file of your samples, mixtures inside this folder present the spectra mix of two or more samples, samples section of reference planetary spectra and template. The intention of the work is to provide a user-friendly program to create spectra mix and to avoid editing data files. Therefore, the data tab has the possibility of inserting individual or multiple data to be included, or excluded, from fitting. Data can be grouped, as a single spectrum, using the function save mixture. Fit options consist of selection and zoom of the spectral area, change step of sampling, and smoothing the spectra. It is also possible to manipulate the weights and the sum of fit parameters. The graphical interface shows the goodness of fit through the difference curve (residual plot). The refined spectrum is plotted immediately in the graphics window (black line) with parameters values inside the tab—in particular, the percent of each single sample inside the total spectrum. The tool can be read up to a maximum of 15 samples simultaneously. Graphs and results can be respectively exported as image and text files to an external program. The aim of the program is to generate a spectra mix; it can be done with two different strategies. The first of these is the automatic fit; automatically, the tool provides the best fit of the loaded data with relative percentages. The second strategy (manual modes) is uploading the data and manually entering the percentages of each single spectrum.

Table A1. Minerals used in evaluating mixing model results in addition to the samples analyzed within this work. Samples are taken from Relab Brown University (<http://www.planetary.brown.edu/relab/> (accessed on 23 June 2021)) and the CRISM spectral library (<https://speclib.rsl.wustl.edu/> (accessed on 4 June 2021)).

Mineral Name	Chemical Formula	Sample/Spectra ID	Database
Magnetite	Fe ₃ O ₂	MG-EAC-002	Relab
Calcite	CaCO ₃	GR-CMP-001	Crism
Illite	(K,H ₃ O)(Al,Mg,Fe) ₂ (Si,Al) ₄ O ₁₀ [(OH) ₂ ,(H ₂ O)]	IL-EAC-001	Relab
Sal-ammoniac	NH ₄ Cl	CL-EAC-049	Relab

Table A2. Combination of minerals used to produce the fit.

Fit 1 (a)	Magnetite 76.2%	Calcite 8.8%	Shortite 6.1%	Illite 5.4%	Sal-ammoniac 3.5%
Fit 2 (b)	Magnetite 77.4%	Calcite 9.5%	Illite 5.7%	Natrite 4.9%	Sal-ammoniac 2.5%
Fit 3 (c)	Magnetite 78.6%	Calcite 9.7%	Illite 5.6%	Nyerereite 3.4%	Sal-ammoniac 2.8%
Fit 4 (d)	Magnetite 77%	Calcite 10.1%	Illite 5.8%	Thermonatrite 4.3%	Sal-ammoniac 2.8%
Fit 5 (e)	Magnetite 74%	Calcite 10.8%	Illite 6.3%	Sal-ammoniac 4.8%	Trona 3.4%

References

- McCord, T.B. *Reflectance Spectroscopy in Planetary Science: Review and Strategy for the Future*; National Aeronautics and Space Administration, Scientific and Technical Information Division USA: Washington, DC, USA, 1988; Volume 493.
- Dalton III, J.B. Spectral behavior of hydrated sulfate salts: Implications for Europa mission spectrometer design. *Astrobiology* **2003**, *3*, 771–784. [[CrossRef](#)]
- Cook, J.C.; Dalle Ore, C.M.; Protopapa, S.; Binzel, R.P.; Cartwright, R.; Cruikshank, D.P.; Earle, A.; Grundy, W.M.; Ennico, K.; Howett, C.; et al. Composition of Pluto’s small satellites: Analysis of New Horizons spectral images. *Icarus* **2018**, *315*, 30–45. [[CrossRef](#)]
- Niles, P.B.; Catling, D.C.; Berger, G.; Chassefière, E.; Ehlmann, B.L.; Michalski, J.R.; Morris, R.; Ruff, S.W.; Sutter, B. Geochemistry of carbonates on Mars: Implications for climate history and nature of aqueous environments. *Space Sci. Rev.* **2013**, *174*, 301–328. [[CrossRef](#)]
- Ehlmann, B.L.; Mustard, J.F.; Murchie, S.L.; Poulet, F.; Bishop, J.L.; Brown, A.J.; Calvin, W.M.; Clark, R.N.; Des Marais, D.J.; Milliken, R.E.; et al. Orbital identification of carbonate-bearing rocks on Mars. *Science* **2008**, *322*, 1828–1832. [[CrossRef](#)] [[PubMed](#)]
- Morris, R.V.; Ruff, S.W.; Gellert, R.; Ming, D.W.; Arvidson, R.E.; Clark, B.C.; Golden, D.C.; Siebach, K.; Klingelhöfer, G.; Schröder, C.; et al. Identification of carbonate-rich outcrops on Mars by the Spirit rover. *Science* **2010**, *329*, 421–424. [[CrossRef](#)] [[PubMed](#)]
- Boynton, W.V.; Ming, D.W.; Kounaves, S.P.; Young, S.M.M.; Arvidson, R.E.; Hecht, M.H.; Hoffman, J.; Niles, P.B.; Hamara, D.K.; Quinn, R.C.; et al. Evidence for calcium carbonate at the Mars Phoenix landing site. *Science* **2009**, *325*, 61–64. [[CrossRef](#)] [[PubMed](#)]
- Carrozzo, F.G.; De Sanctis, M.C.; Raponi, A.; Ammannito, E.; Castillo-Rogez, J.; Ehlmann, B.L.; Marchi, S.; Stein, N.; Ciarniello, M.; Tosi, F.; et al. Nature, formation, and distribution of carbonates on Ceres. *Sci. Adv.* **2018**, *4*, e1701645. [[CrossRef](#)]
- De Sanctis, M.C.; Raponi, A.; Ammannito, E.; Ciarniello, M.; Toplis, M.J.; McSween, H.Y.; Castillo-Rogez, J.C.; Ehlmann, B.L.; Carrozzo, F.G.; Marchi, S.; et al. Bright carbonate deposits as evidence of aqueous alteration on (1) Ceres. *Nature* **2016**, *536*, 54–57. [[CrossRef](#)] [[PubMed](#)]
- De Sanctis, M.C.; Vinogradoff, V.; Raponi, A.; Ammannito, E.; Ciarniello, M.; Carrozzo, F.G.; De Angelis, S.; A Raymond, C.; Russell, C.T. Characteristics of organic matter on Ceres from VIR/Dawn high spatial resolution spectra. *Mon. Not. R. Astron. Soc.* **2019**, *482*, 2407–2421. [[CrossRef](#)]
- Zambon, F.; Raponi, A.; Tosi, F.; De Sanctis, M.C.; McFadden, L.A.; Carrozzo, F.G.; Longobardo, A.; Ciarniello, M.; Krohn, K.; Stephan, K.; et al. Spectral analysis of Ahuna Mons from Dawn mission’s visible-infrared spectrometer. *Geophys. Res. Lett.* **2017**, *44*, 97–104. [[CrossRef](#)]
- De Sanctis, M.C.; Mitri, G.; Castillo-Rogez, J.; House, C.H.; Marchi, S.; Raymond, C.A.; Sekine, Y. Relict Ocean Worlds: Ceres. *Space Sci. Rev.* **2020**, *216*, 1–33. [[CrossRef](#)]
- Castillo-Rogez, J.C.; Neveu, M.; Scully, J.E.; House, C.H.; Quick, L.C.; Bouquet, A.; Miller, K.; Bland, M.; De Sanctis, M.C.; Ermakov, A.; et al. Ceres: Astrobiological target and possible ocean world. *Astrobiology* **2020**, *20*, 269–291. [[CrossRef](#)]
- Postberg, F.; Kempf, S.; Schmidt, J.; Brilliantov, N.; Beinsen, A.; Abel, B.; Buck, U.; Srama, R. Sodium salts in E-ring ice grains from an ocean below the surface of Enceladus. *Nature*, **2009**, *459*, 1098–1101. [[CrossRef](#)] [[PubMed](#)]
- Postberg, F.; Schmidt, J.; Hillier, J.; Kempf, S.; Srama, R. A salt-water reservoir as the source of a compositionally stratified plume on Enceladus. *Nature* **2011**, *474*, 620–622. [[CrossRef](#)]
- Carlson, R.W.; Calvin, W.M.; Dalton, J.B.; Hansen, G.B.; Hudson, R.L.; Johnson, R.E.; McCord, T.B.; Moore, M.H. Europa’s Surface Composition. In *Europa*; Pappalardo, R.T., McKinnon, W.B., Khurana, K.K., Eds.; University of Arizona: Tucson, AZ, USA, 2009; Volume 283.
- McCord, T.B.; Hansen, G.B.; Combe, J.P.; Hayne, P. Hydrated minerals on Europa’s surface: An improved look from the Galileo NIMS investigation. *Icarus* **2010**, *209*, 639–650. [[CrossRef](#)]

18. De Angelis, S.; Carli, C.; Tosi, F.; Beck, P.; Brissaud, O.; Schmitt, B.; Potin, S.; De Sanctis, M.C.; Capaccioni, F.; Piccioni, G. NIR reflectance spectroscopy of hydrated and anhydrous sodium carbonates at different temperatures. *Icarus* **2019**, *317*, 388–411. [[CrossRef](#)]
19. McCord, T.B.; Hansen, G.B.; Matson, D.L.; Johnson, T.V.; Crowley, J.K.; Fanale, F.P.; Carlson, R.W.; Smythe, W.D.; Martin, P.D.; Hibbitts, C.A.; et al. Hydrated salt minerals on Europa's surface from the Galileo near-infrared mapping spectrometer (NIMS) investigation. *J. Geophys. Res. Planets* **1999**, *104*, 11827–11851. [[CrossRef](#)]
20. Gooding, J.L. Chemical weathering on Mars thermodynamic stabilities of primary minerals (and their alteration products) from mafic igneous rocks. *Icarus* **1978**, *33*, 483–513. [[CrossRef](#)]
21. Ehlmann, B.L.; Edwards, C.S. Mineralogy of the Martian surface. *Annu. Rev. Earth Planet. Sci.* **2014**, *42*, 291–315. [[CrossRef](#)]
22. Zolotov, M.Y.; Shock, E.L. Composition and stability of salts on the surface of Europa and their oceanic origin. *J. Geophys. Res. Planets* **2001**, *106*, 32815–32827. [[CrossRef](#)]
23. Fanale, F.P.; Johnson, T.V.; Matson, D.L. Io's surface and the histories of the Galilean satellites. In *Annual Review of Earth and Planetary Sciences*; Annual Reviews, Inc.: Palo Alto, CA, USA, 1978; Volume 6, pp. 93–125.
24. Kargel, J.S. Brine volcanism and the interior structures of asteroids and icy satellites. *Icarus* **1991**, *94*, 368–390. [[CrossRef](#)]
25. Kargel, J.S.; Kaye, J.Z.; Head, J.W., III; Marion, G.M.; Sassen, R.; Crowley, J.K.; Hogenboom, D.L. Europa's crust and ocean: Origin. Composition. and the prospects for life. *Icarus* **2000**, *148*, 2262–2265. [[CrossRef](#)]
26. Kamenetsky, V.S.; Kamenetsky, M.B.; Weiss, Y.; Navon, O.; Nielsen, T.F.; Mernagh, T.P. How unique is the Udachnaya-East kimberlite? Comparison with kimberlites from the Slave Craton (Canada) and SW Greenland. *Lithos* **2009**, *112*, 334–346. [[CrossRef](#)]
27. Vennari, C.E.; Beavers, C.M.; Williams, Q. High-pressure/temperature behavior of the alkali/calcium carbonate shortite ($\text{Na}_2\text{Ca}_2(\text{CO}_3)_3$): Implications for carbon sequestration in Earth's transition zone. *J. Geophys. Res. Solid Earth* **2018**, *123*, 6574–6591. [[CrossRef](#)]
28. Keller, J.; Zaitsev, A.N. Reprint of "Geochemistry and petrogenetic significance of natrocarbonatites at Oldoinyo Lengai, Tanzania: Composition of lavas from 1988 to 2007". *Lithos* **2018**, *152*, 47–55. [[CrossRef](#)]
29. Watkinson, D.H.; Chao, G.Y. Shortite in kimberlite from the Upper Canada gold mine, Ontario. *J. Geol.* **1973**, *81*, 229–233. [[CrossRef](#)]
30. Cooper, A.F.; Gittins, J. Shortite in kimberlite from the upper Canada gold mine, Ontario: A discussion. *J. Geol.* **1974**, *82*, 667–669. [[CrossRef](#)]
31. Stoppa, F.; Jones, A.P.; Sharygin, V.V. Nyerereite from carbonatite rocks at Vulture volcano: Implications for mantle metasomatism and petrogenesis of alkali carbonate melts Research Article. *Cent. Eur. J. Geosci.* **2009**, *1*, 131–151. [[CrossRef](#)]
32. Golovin, A.V.; Sharygin, I.S.; Korsakov, A.V.; Kamenetsky, V.S.; Abersteiner, A. Can primitive kimberlite melts be alkali-carbonate liquids: Composition of the melt snapshots preserved in deepest mantle xenoliths. *J. Raman Spectrosc.* **2020**, *51*, 1849–1867. [[CrossRef](#)]
33. Kaminsky, F.; Wirth, R.; Matsyuk, S.; Schreiber, A.; Thomas, R. Nyerereite and nahcolite inclusions in diamond: Evidence for lower-mantle carbonatitic magmas. *Mineral. Mag.* **2009**, *73*, 797–816. [[CrossRef](#)]
34. Kelektsoğlu, K. Carbon Capture and Storage: A Review of Mineral Storage of CO_2 in Greece. *Sustainability* **2018**, *10*, 4400. [[CrossRef](#)]
35. Deeg, H.J.; Belmonte, J.A. *Handbook of Exoplanets*; Springer: Berlin/Heidelberg, Germany, 2018.
36. Balic-Zunic, T.; Birkedal, R.; Katerinopolou, A.; Comodi, P. Dehydration of bloedite, $\text{Na}_2\text{Mg}(\text{SO}_4)_2(\text{H}_2\text{O})_4$ and leonite $\text{K}_2\text{Mg}(\text{SO}_4)_2(\text{H}_2\text{O})_4$. *Eur. J. Mineral.* **2016**, *28*, 133–142. [[CrossRef](#)]
37. Comodi, P.; Stagno, V.; Zucchini, A.; Fei, Y.W.; Prakapenka, V. The compression behavior of blodite at low and high temperature up to similar to 10 GPa: Implications for the stability of hydrous sulphates on icy planetary bodies. *Icarus* **2017**, *285*, 137–144. [[CrossRef](#)]
38. Comodi, P.; Fastelli, M.; Maturilli, A.; Balic-Zunic, T.; Zucchini, A. Emissivity and reflectance spectra at different temperatures of hydrated and anhydrous sulphates: A contribution to investigate the composition and dynamic of icy planetary bodies. *Icarus* **2021**, *355*, 114132. [[CrossRef](#)]
39. Comodi, P.; Nazzareni, S.; Balić-Žunić, T.; Zucchini, A.; Hanfland, M. The high-pressure behavior of bloedite: A synchrotron single-crystal X-ray diffraction study. *Am. Mineral.* **2014**, *99*, 511–518. [[CrossRef](#)]
40. Harner, P.L.; Gilmore, M.S. Visible–near infrared spectra of hydrous carbonates, with implications for the detection of carbonates in hyperspectral data of Mars. *Icarus* **2015**, *250*, 204–214. [[CrossRef](#)]
41. Gaffey, S.J. Spectral reflectance of carbonate minerals in the visible and near infrared (0.35–2.55 μm): Anhydrous carbonate minerals. *J. Geophys. Res. Solid Earth* **1987**, *92*, 1429–1440. [[CrossRef](#)]
42. Meeke, H.; Rasing, T.; Wyder, P.; Janner, A.; Janssen, T. Raman and infrared spectra of the incommensurate crystal Na_2CO_3 . *Phys. Rev. B* **1986**, *34*, 4240. [[CrossRef](#)]
43. Harris, M.J.; Salje, E.K.H. The incommensurate phase of sodium carbonate: An infrared absorption study. *J. Phys. Condens. Matter* **1992**, *4*, 4399. [[CrossRef](#)]
44. Golovin, A.V.; Korsakov, A.V.; Gavryushkin, P.N.; Zaitsev, A.N.; Thomas, V.G.; Moine, B.N. Raman spectra of nyerereite, gregoryite, and synthetic pure $\text{Na}_2\text{Ca}(\text{CO}_3)_2$: Diversity and application for the study micro inclusions. *J. Raman Spectrosc.* **2017**, *48*, 1559–1565. [[CrossRef](#)]

45. Palomba, E.; Longobardo, A.; De Sanctis, M.C.; Stein, N.T.; Ehlmann, B.; Galiano, A.N.; Raponi, A.; Ciarniello, M.; Ammannito, E.; Cloutis, E.; et al. Compositional differences among Bright Spots on the Ceres surface. *Icarus* **2019**, *320*, 202–212. [[CrossRef](#)]
46. Hapke, B. Bidirectional reflectance spectroscopy: 1. Theory. *J. Geophys. Res. Solid Earth* **1981**, *86*, 3039–3054. [[CrossRef](#)]
47. Hapke, B. Bidirectional reflectance spectroscopy 7: The single particle phase function hockey stick relation. *Icarus* **2012**, *221*, 1079–1083. [[CrossRef](#)]
48. Scheetz, B.E.; White, W.B. Vibrational spectra of the alkaline earth double carbonates. *Am. Mineral.* **1977**, *62*, 36–50.
49. Frost, R.L.; Palmer, S.J. Infrared and infrared emission spectroscopy of nesquehonite $\text{Mg}(\text{OH})(\text{HCO}_3) \cdot 2\text{H}_2\text{O}$ —implications for the formula of nesquehonite. *Spectrochim. Acta Part A Mol. Biomol. Spectrosc.* **2011**, *78*, 1255–1260. [[CrossRef](#)]
50. Clark, R.N.; King, T.V.V.; Klejwa, M.; Swayze, G.A.; Vergo, N. High spectral resolution reflectance spectroscopy of minerals. *J. Geophys. Res. Solid Earth* **1990**, *95*, 12653–12680. [[CrossRef](#)]
51. Zhu, Y.; Li, Y.; Ding, H.; Lu, A.; Li, Y.; Wang, C. Infrared emission properties of a kind of natural carbonate: Interpretation from mineralogical analysis. *Phys. Chem. Miner.* **2020**, *47*, 1–15. [[CrossRef](#)]
52. Kolesov, B.A.; Geiger, C.A. The orientation and vibrational states of H_2O in synthetic alkali-free beryl. *Phys. Chem. Miner.* **2000**, *27*, 557–564. [[CrossRef](#)]
53. Yamatera, H.; Fitzpatrick, B.; Gordon, G. Near infrared spectra of water and aqueous solutions. *J. Mol. Spectrosc.* **1964**, *14*, 268–278. [[CrossRef](#)]
54. Bayly, J.G.; Kartha, V.B.; Stevens, W.H. The absorption spectra of liquid phase H_2O , HDO and D_2O from 0.7 μm to 10 μm . *Infrared Phys.* **1963**, *3*, 211–223. [[CrossRef](#)]
55. Cloutis, E.A.; Hawthorne, F.C.; Stanley, A.; Mertzman, K.K.; Michael, A.C.; Dionne, M.; Michelle Methot, J.S.; John, F.M.; Diana, L.B.; James III, F.B.; et al. Detection and discrimination of sulphate minerals using reflectance spectroscopy. *Icarus* **2006**, *184*, 121–157. [[CrossRef](#)]
56. Moenke, H.H.W. Vibrational spectra and the crystal-chemical classification of minerals. In *The Infrared Spectra of Minerals*; White, W.B., Farmer, V.C., Eds.; Mineralogical Society Monograph: London, UK, 1974; pp. 111–118.
57. Bishop, J.L.; Dyar, M.D.; Lane, M.D.; Banfield, J.F. Spectral identification of hydrated sulfates on Mars and comparison with acidic environments on Earth. *Int. J. Astrobiol.* **2004**, *3*, 275–285. [[CrossRef](#)]
58. Maturilli, A.; Helbert, J.; John, J.M.S.; Head, J.W., III; Vaughan, W.M.; D’Amore, M.; Gottschalk, M.; Ferrari, S. Komatiites as Mercury surface analogues: Spectral measurements at PEL. *Earth Planet. Sci. Lett.* **2014**, *398*, 58–65. [[CrossRef](#)]
59. Maturilli, A.; Helbert, J.; Arnold, G. The newly improved set-up at the Planetary Spectroscopy Laboratory (PSL). In *Infrared Remote Sensing and Instrumentation XXVII*; SPIE Optical Engineering Applications: San Diego, CA, USA, 2019; Volume 11128, p. 111280T.
60. Rietveld, H.M. A profile refinement method for nuclear and magnetic structures. *J. Appl. Crystallogr.* **1969**, *2*, 65–71. [[CrossRef](#)]
61. Larson, A.C.; Von Dreele, R.B. *Generalized Structure Analysis System*; University of California: San Diego, CA, USA, 1988.
62. Toby, B.H. EXPGUI, a graphical user interface for GSAS. *J. Appl. Crystallogr.* **2001**, *34*, 210–213. [[CrossRef](#)]
63. Downs, R.T.; Hall-Wallace, M. The American Mineralogist crystal structure database. *Am. Mineral.* **2003**, *88*, 247–250.
64. Palmer, D.C. *CrystalMaker*; CrystalMaker Software Ltd: Begbroke, Oxfordshire, UK, 2014.
65. Dollase, W.A. Correction of intensities for preferred orientation in powder diffractometry: Application of the March model. *J. Appl. Crystallogr.* **1986**, *19*, 267–272. [[CrossRef](#)]
66. Adler, H.H.; Kerr, P.F. Infrared spectra, symmetry and structure relations of some carbonate minerals. *Am. Mineral.* **1963**, *48*, 839–853.
67. Zubkova, N.V.; Pushcharovsky, D.Y.; Ivaldi, G.; Ferraris, G.; Pekov, I.V.; Chukanov, N.V. Crystal structure of natrite, $\gamma\text{-Na}_2\text{CO}_3$. *Neues Jahrb. Für Mineral. Monatshefte* **2002**, *2*, 85–96. [[CrossRef](#)]
68. Dušek, M.; Chapuis, G.; Meyer, M.; Petricek, V. Sodium carbonate revisited. *Acta Crystallogr. Sect. B Struct. Sci.* **2003**, *59*, 337–352. [[CrossRef](#)]
69. Arakcheeva, A.; Bindi, L.; Pattison, P.; Meisser, N.; Chapuis, G.; Pekov, I. The incommensurately modulated structures of natural natrite at 120 and 293 K from synchrotron X-ray data. *Am. Mineral.* **2010**, *95*, 574–581. [[CrossRef](#)]
70. Arakcheeva, A.; Chapuis, G. A reinterpretation of the phase transitions in Na_2CO_3 . *Acta Crystallogr. Sect. B Struct. Sci.* **2005**, *61*, 601–607. [[CrossRef](#)] [[PubMed](#)]
71. Swainson, I.P.; Dove, M.T.; Harris, M.J. Neutron powder diffraction study of the ferroelastic phase transition and lattice melting in sodium carbonate, Na_2CO_3 . *J. Phys. Condens. Matter* **1995**, *7*, 4395. [[CrossRef](#)]
72. Gavryushkin, P.N.; Thomas, V.G.; Bolotina, N.B.; Bakakin, V.V.; Golovin, A.V.; Seryotkin, Y.V.; Fursenko, D.A.; Litasov, K.D. Hydrothermal synthesis and structure solution of $\text{Na}_2\text{Ca}(\text{CO}_3)_2$: “synthetic analogue” of mineral nyerereite. *Cryst. Growth Des.* **2016**, *16*, 1893–1902. [[CrossRef](#)]
73. Song, Y.; Luo, M.; Zhao, D.; Peng, G.; Lina, C.; Ye, N. Explorations of new UV nonlinear optical materials in the $\text{Na}_2\text{CO}_3\text{-CaCO}_3$ system. *J. Mater. Chem. C* **2017**, *5*, 8758. [[CrossRef](#)]
74. Dickens, B.; Hyman, A.; Brown, W.E. Crystal structure of $\text{Ca}_2\text{Na}_2(\text{CO}_3)_3$ (shortite). *J. Res. Natl. Bur. Stand. Sec. A Phys. Chem. A* **1971**, *75*, 129–140. [[CrossRef](#)]
75. Dickens, B.; Mauer, F.A.; Brown, W.E. A Refinement of the Crystal Structure of $\text{Na}_2\text{CO}_3 \cdot \text{H}_2\text{O}$. *J. Res. Natl. Bur. Standards. Sect. A Phys. Chem.* **1970**, *74*, 319–324. [[CrossRef](#)]

76. Wu, K.K.; Brown, I.D. A neutron diffraction study of $\text{Na}_2\text{CO}_3 \cdot \text{H}_2\text{O}$. *Acta Crystallogr. Sect. B: Struct. Crystallogr. Cryst. Chem.* **1975**, *31*, 890–892. [[CrossRef](#)]
77. Hartman, M.; Trnka, O.; Vesely, V.; Svoboda, K. Thermal dehydration of the sodium carbonate hydrates. *Chem. Eng. Commun.* **2001**, *185*, 1–16. [[CrossRef](#)]
78. O'Bannon, E., III; Beavers, C.M.; Williams, Q. Trona at extreme conditions: A pollutant-sequestering material at high pressures and low temperatures. *Am. Mineral.* **2014**, *99*, 1973–1984. [[CrossRef](#)]
79. Brown, C.J.; Peiser, H.S.; Turner-Jones, A. The Crystal Structure of Sodium Sesquicarbonate. *Acta Crystallogr.* **1949**, *2*, 167. [[CrossRef](#)]
80. Choi, C.S.; Mighell, A.D. Neutron diffraction study of sodium sesquicarbonate dihydrate. *Acta Crystallogr. Sect. B: Struct. Crystallogr. Cryst. Chem.* **1982**, *38*, 2874–2876. [[CrossRef](#)]
81. Barall, E.M., II; Rogers, L.B. Differential thermal analysis of the decomposition of sodium bicarbonate and its simple double salts. *J. Inorg. Nucl. Chem.* **1966**, *28*, 41–51. [[CrossRef](#)]
82. Bultel, B.; Viennet, J.C.; Poulet, F.; Carter, J.; Werner, S.C. Detection of carbonates in Martian weathering profiles. *J. Geophys. Res. Planets* **2019**, *124*, 989–1007. [[CrossRef](#)]
83. Huang, C.K.; Kerr, P.F. Infrared study of the carbonate minerals. *Am. Mineral.* **1960**, *45*, 311–324.
84. Frost, R.L.; Dickfos, M.J. Raman and infrared spectroscopic study of the anhydrous carbonate minerals shortite and barytocalcite. *Spectrochim. Acta A Mol. Biomol. Spectrosc.* **2008**, *71*, 143–146. [[CrossRef](#)] [[PubMed](#)]
85. Hartley, M.; MacLennan, J. Magmatic densities control erupted volumes in Icelandic volcanic systems. *Front. Earth Sci.* **2018**, *6*, 29. [[CrossRef](#)]
86. De Sanctis, M.C.; Ammannito, E.; Raponi, A.; Marchi, S.; McCord, T.B.; McSween, H.Y.; Longobardo, A. Ammoniated phyllosilicates with a likely outer Solar System origin on (1) Ceres. *Nature* **2015**, *528*, 2412–2444. [[CrossRef](#)] [[PubMed](#)]
87. Schröder, S.E.; Poch, O.; Ferrari, M.; De Angelis, S.; Sultana, R.; Potin, S.M.; Beck, P.; De Sanctis, M.C.; Schmitt, B. Dwarf planet (1) Ceres surface bluing due to high porosity resulting from sublimation. *Nat. Commun.* **2012**, *12*, 1–9.
88. McSween, H.Y., Jr.; Emery, J.P.; Rivkin, A.S.; Toplis, M.J.; Castillo-Rogez, J.C.; Prettyman, T.H.; Russell, C.T. Carbonaceous chondrites as analogs for the composition and alteration of Ceres. *Meteorit. Planet. Sci.* **2018**, *53*, 1793–1804. [[CrossRef](#)]
89. Schenk, P.; Sizemore, H.; Schmidt, B.; Castillo-Rogez, J.; De Sanctis, M.; Bowling, T.; Scully, J.; Buczkowski, D.; Quick, L.; Preusker, F.; et al. The central pit and dome at Cerealia Facula bright deposit and floor deposits in Occator crater, Ceres: Morphology, comparisons and formation. *Icarus* **2019**, *320*, 159–187. [[CrossRef](#)]
90. Russell, C.T.; Raymond, C.A.; Ammannito, E.; Buczkowski, D.L.; De Sanctis, M.C.; Hiesinger, H.; Yamashita, N. Dawn arrives at Ceres: Exploration of a small, volatile-rich world. *Science* **2016**, *353*, 1008–1010. [[CrossRef](#)] [[PubMed](#)]
91. Schenk, P.; Scully, J.; Buczkowski, D.; Sizemore, H.; Schmidt, B.; Pieters, C.; Raymond, C. Impact heat driven volatile redistribution at Occator crater on Ceres as a comparative planetary process. *Nat. Commun.* **2020**, *11*, 1–11. [[CrossRef](#)]
92. Ruesch, O.; Platz, T.; Schenk, P.; McFadden, L.A.; Castillo-Rogez, J.C.; Quick, L.C.; Byrne, S.; Preusker, F.; O'Brien, D.P.; Schmedemann, N.; et al. Cryovolcanism on Ceres. *Science* **2016**, *353*, aaf4286. [[CrossRef](#)] [[PubMed](#)]
93. Bu, C.; Lopez, G.R.; Dukes, C.A.; McFadden, L.A.; Li, J.Y.; Ruesch, O. Stability of hydrated carbonates on Ceres. *Icarus* **2019**, *320*, 136–149. [[CrossRef](#)]
94. Zucchini, A.; Prencipe, M.; Belmonte, D.; Comodi, P. Ab initio study of the dolomite to dolomite II high pressure phase transition. *Eur. J. Mineral.* **2017**, *29*, 227–238. [[CrossRef](#)]
95. Zucchini, A.; Comodi, P.; Nazzareni, S.; Hanfland, M. The effect of cation ordering and temperature on the high-pressure behaviour of dolomite. *Phys. Chem. Miner.* **2014**, *41*, 783–793. [[CrossRef](#)]
96. Nakamura, R.; Ohtani, E. The high-pressure phase relation of the $\text{MgSO}_4\text{--H}_2\text{O}$ system and its implication for the internal structure of Ganymede. *Icarus* **2011**, *211*, 648–654. [[CrossRef](#)]
97. Journaux, B.; Kalousov'a, K.; Sotin, C.; Tobie, G.; Vance, S.; Saur, J.; Bollengier, O.; Noack, L.; Rückriemen-Bez, T.; Van Hoolst, T.; et al. Large ocean worlds with high-pressure ices. *Space Sci. Rev.* **2020**, *216*, 1–36. [[CrossRef](#)]
98. Bevington, P.R.; Robinson, D.K.; Blair, J.M.; Mallinckrodt, A.J.; McKay, S. Data reduction and error analysis for the physical sciences. *Comput. Phys.* **1993**, *7*, 415–416. [[CrossRef](#)]